

Special Section:

ExoMars Trace Gas Orbiter - One Martian Year of Science

Key Points:

- Retrieval of Martian aerosols key properties from NOMAD-SO data during the MY 34 GDS
- Mesospheric dust and water ice r_{eff} are mainly $\sim 1 \mu\text{m}$ and $\leq 0.5 \mu\text{m}$ respectively during the MY 34 GDS and its decay phase
- During the MY 34 GDS, the effective variance shows a slight N/S asymmetry and values mainly ≤ 0.2

Correspondence to:

A. Stolzenbach,
aurelien.stolzenbach@gmail.com

Citation:

Stolzenbach, A., López Valverde, M.-A., Brines, A., Modak, A., Funke, B., González-Galindo, F., et al. (2023). Martian atmospheric aerosols composition and distribution retrievals during the first Martian year of NOMAD/TGO solar occultation measurements: 1. Methodology and application to the MY 34 global dust storm. *Journal of Geophysical Research: Planets*, 128, e2022JE007276. <https://doi.org/10.1029/2022JE007276>

Received 1 MAR 2022
 Accepted 26 JUN 2023

Author Contributions:
















Conceptualization: Aurélien Stolzenbach, Miguel-Angel López Valverde, Bernd Funke
Formal analysis: Aurélien Stolzenbach, Bernd Funke
Investigation: Aurélien Stolzenbach, Miguel-Angel López Valverde
Methodology: Aurélien Stolzenbach, Miguel-Angel López Valverde
Resources: Miguel-Angel López Valverde, Francisco González-Galindo
Software: Aurélien Stolzenbach, Bernd Funke

© 2023. The Authors.

This is an open access article under the terms of the [Creative Commons Attribution-NonCommercial-NoDerivs License](https://creativecommons.org/licenses/by/4.0/), which permits use and distribution in any medium, provided the original work is properly cited, the use is non-commercial and no modifications or adaptations are made.



Martian Atmospheric Aerosols Composition and Distribution Retrievals During the First Martian Year of NOMAD/TGO Solar Occultation Measurements: 1. Methodology and Application to the MY 34 Global Dust Storm

Aurélien Stolzenbach¹ , Miguel-Angel López Valverde¹ , Adrian Brines¹ , Ashimananda Modak¹ , Bernd Funke¹ , Francisco González-Galindo¹ , Ian Thomas² , Giuliano Liuzzi³ , Gerónimo Villanueva⁴ , Mikhail Luginin⁵ , Shohei Aoki^{2,6} , Udo Grabowski⁷, José Juan Lopez Moreno¹, Julio Rodríguez Gómez¹, Mike Wolff⁸ , Bojan Ristic² , Frank Daerden² , Giancarlo Bellucci⁹, Manish Patel¹⁰ , and Ann-Carine Vandaele²

¹Instituto de Astrofísica de Andalucía, Granada, Spain, ²Belgian Royal Institute for Space Aeronomy, Brussels, Belgium, ³School of Engineering, University of Basilicata, Potenza, Italy, ⁴NASA Goddard Space Flight Center, Greenbelt, MD, USA, ⁵Space Research Institute (IKI), Moscow, Russia, ⁶Japan Aerospace Exploration Agency (JAXA), Tokyo, Japan, ⁷Karlsruhe Institute of Technology, Institute of Meteorology and Climate Research, Karlsruhe, Germany, ⁸Space Science Institute, Boulder, CO, USA, ⁹Institute for Space Astrophysics and Planetology, Rome, Italy, ¹⁰Open University, Milton Keynes, UK

Abstract Since the beginning of the Trace Gas Orbiter (TGO) science operations in April 2018, its instrument “Nadir and Occultation for Mars Discovery” (NOMAD) supplies detailed observations of the IR spectrums of the Martian atmosphere. We developed a procedure that allows us to evaluate the composition and distribution's parameters of the atmospheric Martian aerosols. We use a retrieval program (RCP) in conjunction with a radiative forward model (KOPRA) to evaluate the vertical profile of aerosol extinction from NOMAD measurements. We then apply a model/data fitting strategy of the aerosol extinction. In this first article, we describe the method used to evaluate the parameters representing the Martian aerosol composition and size distribution. MY 34 GDS showed a peak intensity from L_S 190° to 210°. During this period, the aerosol content rises multiple scale height, reaching altitudes up to 100 km. The lowermost altitude of aerosol's detection during NOMAD observation rises up to 30 km. Dust aerosols r_{eff} were observed to be close to 1 μm and its ν_{eff} lower than 0.2. Water ice aerosols r_{eff} were observed to be submicron with a ν_{eff} lower than 0.2. The vertical aerosol structure can be divided in two parts. The lower layers are represented by higher r_{eff} than the upper layers. The change between the lower and upper layers is very steep, taking only few kilometers. The decaying phase of the GDS, L_S 210°–260°, shows a decrease in altitude of the aerosol content but no meaningful difference in the observed aerosol's size distribution parameters.

Plain Language Summary Mars' atmosphere is filled with dust and water ice particles carried by the winds. These aerosols affect the way sunlight is distributed in the atmosphere and on the surface, and this directly affects temperature. In addition, approximately every three Martian years, Mars experiences what is known as a “global dust storm.” This type of dust storm covers the entire red planet in dust. It affects the temperature and water vapor content of the Martian atmosphere. Determining and assessing aerosol properties, number, size and mass during and after a global dust storm is of crucial importance to understanding its underlying mechanisms. Here, we develop an analysis scheme to study the size, nature, number and distribution of Martian aerosols. Our study confirms that, overall, dust and water ice particles are quite small, close to 1 μm or even smaller, and that a global dust storm affects the intensity of other storms that follow.

1. Introduction

The climate of all planets is strongly influenced by the aerosols present in their atmosphere. Their nature, size distribution and content affect the energy balance, and therefore the atmospheric dynamics of the planet. On Mars, we know that there are three types of aerosol: dust, water ice and carbon dioxide ice. Dust affects the thermal structure of the Martian atmosphere through radiative heating (Davies, 1979; Forget et al., 1999; Kleinböhl et al., 2009, 2011; Smith, 2004). Water ice has a broader effect than dust, since it affects both the thermal structure, by modifying the radiative balance (Wilson et al., 2008; Madeleine et al., 2012; T. Navarro et al., 2014),

Supervision: Miguel-Angel López Valverde

Validation: Aurélien Stolzenbach, Miguel-Angel López Valverde

Visualization: Aurélien Stolzenbach

Writing – original draft: Aurélien Stolzenbach

Writing – review & editing: Miguel-Angel López Valverde

and the Martian water cycle (Clancy et al., 2017; Montmessin et al., 2004, 2017; Richardson & Wilson, 2002). Condensation of carbon dioxide ice occurs mainly near the poles in winter (polar night) or at high altitude (Clancy et al., 2017; Gary-Bicas et al., 2020; Hayne et al., 2012; Kieffer et al., 2000; Montmessin et al., 2007) and may be linked to specific dynamic features (Colaprete et al., 2005; Kuroda et al., 2013). Water and carbon dioxide ices also influence dust content and size distribution through their condensation on smaller dust particles acting as condensation nuclei (T. Navarro et al., 2014).

This article is divided in two parts. The first, presented in the present paper, focuses on the method of recovering Martian aerosol properties and its results for the Martian Global Dust Storm of Martian year 34 (MY 34). The second part of the article, referred as Paper II in the present paper, extends the results to the end of MY 34 to the first half of MY 35 (Stolzenbach et al., 2023). The Martian atmosphere is affected by events called Global Dust Storms (referred as GDS in deference of Haberle et al. (2017)). As noted in Kahre et al. (2017), GDS are “the most dramatic and thermodynamically significant dust events.” Dust is lifted over several scale heights across Mars, affecting the temperature vertical profile with mid-level altitudes as 20K warmer compared to non GDS years (Smith et al., 2006). A GDS occurs on average one out of three Martian years (Clancy et al., 2000; Kass et al., 2016; Martin & Zurek, 1993) even if the physical exact mechanisms behind it is still unknown. The onset, starting location, intensity, and duration of GDS varies, from initiation at L_S 180° to later solstitial initiation, starting in the southern or northern hemisphere, spanning months or weeks. During MY 34, a northern regional dust storm started at L_S 180°, a few months after the start of TGO science operations, and another regional dust storm at L_S 186° in the southern hemisphere. Later, at L_S 193°, a full GDS appears from these initial storms (Bertrand et al., 2020; Guzewich et al., 2019; Sánchez-Lavega et al., 2019; Smith, 2019). The MY 34 GDS starts to gradually decay from the poles at L_S 205° until $L_S \sim 260^\circ$ of the same Martian year (Kass et al., 2020).

The nature and distribution of Martian aerosols have been observed using many different methods and experiments, from rovers to satellites. An exhaustive review can be found in Haberle et al. (2017) or in Clancy et al. (2019). Typically, dust effective radius, r_{eff} , ranges from 1 to 1.8 μm and its effective variance, ν_{eff} , from 0.2 to 0.4. $\text{H}_2\text{O}_{\text{ice}}$ effective radius ranges from 1 to 5 μm and its effective variance from 0.1 to 0.4. These values being characteristic of a non-GDS Martian year (Chassefière et al., 1992; Clancy et al., 2003, 2019; Fedorova et al., 2009).

As mentioned above, the atmospheric content of aerosols and their characterization are of a crucial importance to atmospheric science. To understand Mars' climate, we need to better characterize and quantify Martian aerosols, especially during events such as GDS. The ExoMars Trace Gas Orbiter mission (TGO) (ESA/Roscosmos) was primarily designed to study trace gases, thermal structure, and aerosol content of the Martian atmosphere with unprecedented vertical resolution (Vago et al., 2015). A previous study by Liuzzi et al. (2020) retrieved the size and abundance of dust and water ice particle from an inversion method using Nadir and Occultation for MArS Discovery Solar Occultation channel (NOMAD-SO) data. Their work used a fixed effective variance but provided significant insight into the challenges of simultaneously extracting dust and water ice information from NOMAD-SO observations. In addition, Liuzzi et al. (2020) demonstrated the strong vertical gradient of the water ice effective radius in the troposphere, as well as its diurnal variability.

In the first part of this article, we present our study of the nature and composition of Martian aerosols during the MY 34 GDS using the NOMAD experiment onboard TGO. In Section 2 we present the NOMAD experiment and data set used in this study. In Section 3, we present our method to retrieve the vertical extinction profiles from NOMAD data. In Section 4 we present our method for evaluating key parameters of Martian aerosol distribution from retrieved extinctions. This follows on directly from Luginin et al. (2020) which studied the nature and distribution of Martian aerosols during the MY 34 GDS using the Atmospheric Chemistry Suite experiment (ACS) also onboard TGO (Korablev et al., 2017). In Section 5, we will present and discuss our results, comparing them with current knowledge and recent studies available from TGO, as reported in Luginin et al. (2020), Liuzzi et al. (2020), and Stcherbinine et al. (2020).

2. NOMAD Data Set

2.1. NOMAD Experiment Onboard TGO

NOMAD is a suite of three spectrometers onboard TGO, covering the spectral ranges from the UV and the visible to the IR, from 0.2 to 4.3 μm (Vandaele et al., 2018). The instrument has two IR spectrometers composed by the

Table 1
Set of Selected NOMAD-SO Diffraction Orders

Order	121	134	149	168	190
Wavelength	3.66 μm	3.31 μm	2.97 μm	2.64 μm	2.33 μm

Solar Occultation channel (SO), operating in the spectral range between 2.3 and 4.3 μm (2,320–4,350 cm^{-1}), the Limb Nadir Occultation channel (LNO) and a third one operating in the UV-visible (UVIS), capable of both nadir and solar occultation observations. The SO channel has been designed like the Solar Occultation in the InfraRed (SOIR) instrument onboard *Venus Express*. It uses an echelle grating with a density of ≈ 4 lines/mm in a Littrow configuration. An Acousto-Optical Tunable Filter (AOTF) is used to select different spectral windows (with a width that varies from 20–35 cm^{-1}). Each window corresponds to the desired diffraction order to be used during the atmospheric scan. The spectral resolution of the SO channel is $\lambda/\Delta\lambda = 20,000$. The time sampling of this channel is approximately of 1 s, allowing a vertical sampling about 1 km. The AOTF also allows a quick change between diffraction orders. As a result, the SO channel can observe the atmosphere at a given altitude with any combination of 6 different diffraction order.

2.2. SO Observations

For our study, we selected a configuration of 5 diffraction orders (cf., Table 1) spanning the overall spectral range, from 2.3 to 3.7 μm , of NOMAD. These orders were selected because they were extensively used together in a large fraction of NOMAD solar occultation observations during the first year of the mission. They also cover a broad spectral range, essential for a good characterization of the aerosol composition. Like Liuzzi et al. (2020), we avoid the orders that has strong CO_2 absorption (typically orders 164 and 165, respectively 2.70 and 2.69 μm) since it alters the capacity of retrieving the aerosol absorption continuum. Our data set starts at MY 34 L_S 180° and ends at MY 35 L_S 180°, covering a full Martian year and the MY 34 GDS. It represents 563 vertical scans with the 5 diffraction orders selected present in each one.

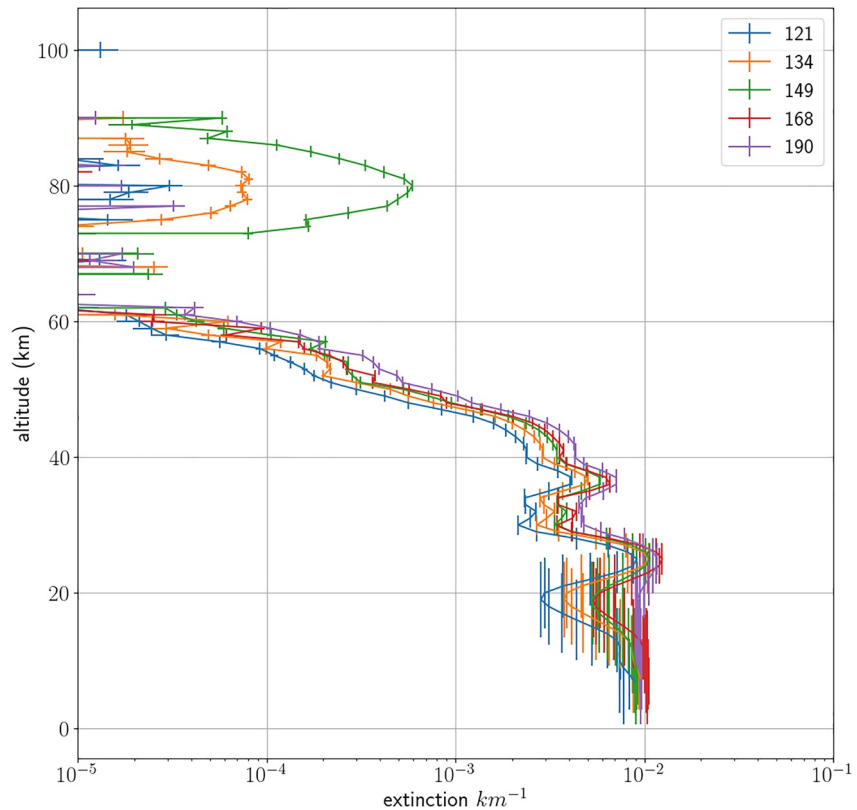


Figure 1. Retrieved extinction vertical profiles from orbit 20180625_050514_1p0a_SO_A_E. The absolute error of the extinction and the vertical resolution are respectively plotted at each altitude point horizontally and vertically.

3. Extinctions Retrievals

We derive the aerosol properties from the broadband behavior of the extinction (units in km^{-1}) at specific wavelengths. To retrieve the extinction, we start with NOMAD level 1 calibrated transmittance data.

3.1. Analysis of NOMAD SO Channel Transmission Profiles

We are using the level 1a transmittance spectrums (Trompet et al., 2023) provided by the PI team at the Belgian Royal Institute of Spatial Aeronomy (BIRA). These calibrated transmittances need to be furthermore processed to correct four prominent features: the Instrument Line Shape (ILS), the AOTF response, a signal spectral shift and continuum curvature. At the Instituto de Astrofísica de Andalucía (IAA), we developed an in-house preprocessing program that evaluates the latter two features, the spectral shift and continuum curvature. To do so, we are using a radiative forward model named KOPRA (Karlsruhe OPTimized Radiative transfer Algorithm described in Stiller et al. (1998)). The preprocessing program postulates the transmittance follows Equation 1 where T is the NOMAD level 1a transmittance data, $\Delta\lambda$ is the spectral shift, T_0 is the KOPRA evaluated transmittance at the same altitude for a reference atmosphere, d is a density scale factor, T_b is an evaluated transmittance due to a polynomial continuum curvature and τ is the evaluated slant opacity.

$$T(\lambda + \Delta\lambda) = T_0^d(\lambda) T_b(\lambda) e^{-\tau} \quad (1)$$

The reference atmosphere is taken from the Mars Planetary Climate Model (Mars PCM) (Forget et al., 1999) for an exact location and season as the NOMAD data. The forward radiative transfer model KOPRA uses HITRAN 2016 (Gordon et al., 2017) spectral lines absorption data for relevant gases in each order (CO_2 , CO , and H_2O mainly). We then evaluate the best set of parameters (d , $\Delta\lambda$, τ) using a sequential brute force calculation, on nested grids of the parameter space, to speed up the calculations. The continuum curvature is evaluated by fitting a 4th order polynomial to the signal continuum. The orders used in this work have also been exploited by our team for deriving temperature, water vapor and carbon monoxide profiles, and a quantitative description of the correction of these features by our pre-processing can be found in a few companion papers (Brines et al., 2022; López Valverde et al., 2022; Modak et al., 2023).

A first attempt to characterize the AOTF and ILS responses signatures was performed during in-flight calibrations. More recently, the NOMAD calibration team has revisited the calibration, improving the characterization

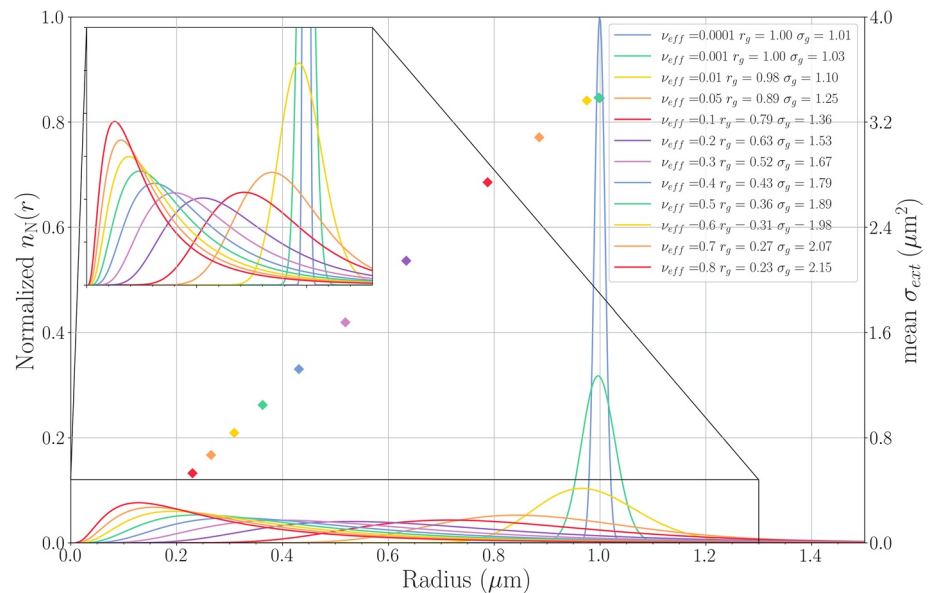


Figure 2. Curves of several log-normal distributions with fixed effective radius $r_{\text{eff}} = 1 \mu\text{m}$ for variable effective variances ν_{eff} . Dust mean extinction cross-sections σ_{ext} at $2.38 \mu\text{m}$ are shown with diamonds shape markers. Their values are reported onto the right y-axis in (μm^2) . Their positions on the x-axis represent the actual value of the median radius \bar{r}_g for the corresponding log-normal. The values of the parameters defining the log-normal (\bar{r}_g, σ_g) are also reported in the legend box.

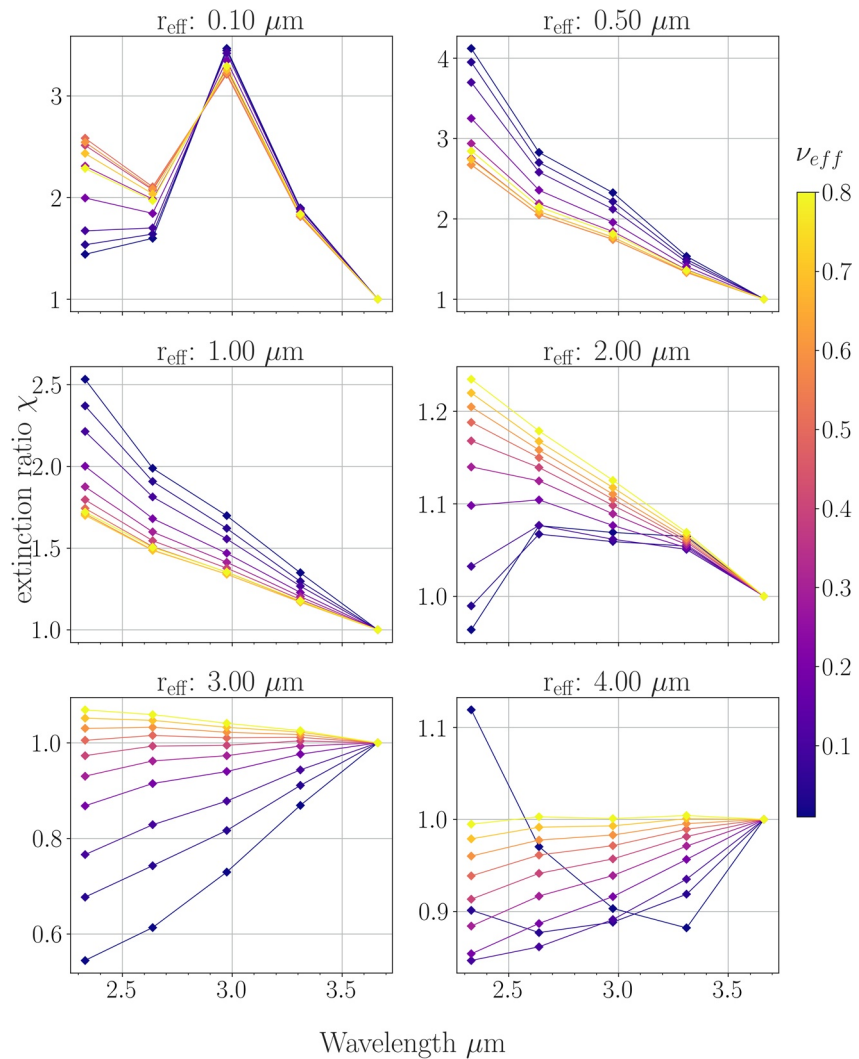


Figure 3. Dust extinction ratios including the 5 diffraction orders used in this work using a reference extinction at $\lambda_0 = 3.66 \mu\text{m}$ (order 121). See text for details.

of the AOTF with Sun observations. BIRA, Goddard and IAA teams worked at a common solution for the ILS and AOTF. The AOTF updated calibration presented in Villanueva et al. (2022) describes the AOTF response with an asymmetric sinc function added to a Gaussian, operating as an offset. The parameters that describe the AOTF are wavenumber dependent. The ILS can be described by an addition of two Gaussian functions with a separation and a scaling ratio between them that varies across the diffraction orders. In this work we use the recommended values for the orders displayed in Table 1.

3.2. Extinctions Inversion Using RCP

RCP stands for Retrieval Control Program, it is a multi-parameter non-linear least squares fitting of measured and modeled spectra (von Clarmann et al., 2003). The forward model incorporated in this level-2 processor is the state-of-the-art line by line radiative transfer model called KOPRA (Stiller et al., 1998). KOPRA was recently adapted to limb emissions on Mars (Jiménez-Monferrer et al., 2021), and for this work it has been adapted to solar occultation data on Mars for the first time, and to the NOMAD SO channel with implementation of the asymmetric AOTF transfer function and the double Gaussian ILS. The inputs to RCP are the initial guess and a priori information of the quantities to be retrieved, as well as the NOMAD level 1a measured spectra preprocessed by our in-house program described in Section 3.1. Regarding the aerosols, the first guess and a priori are

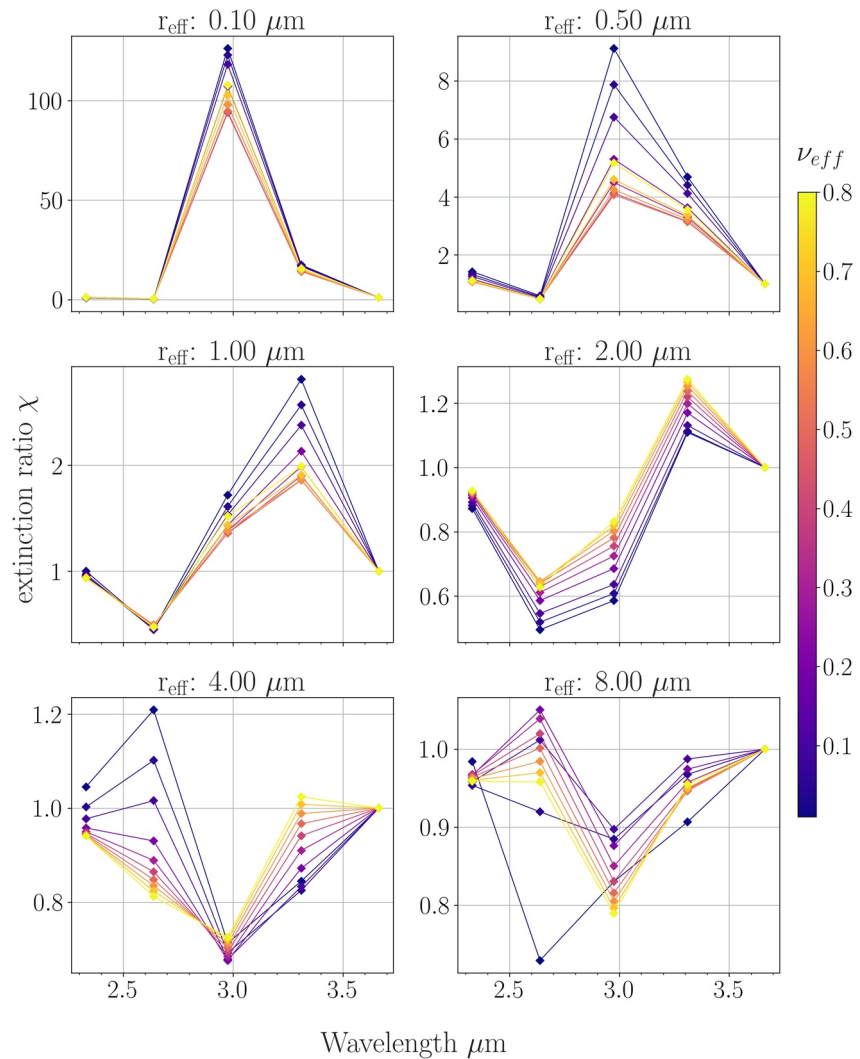


Figure 4. H₂O ice extinction ratios including the 5 diffraction orders using a reference extinction at $\lambda_0 = 3.66 \mu\text{m}$ (order 121). See text for details.

always a null vertical profile of the extinction. RCP solves iteratively the inverse problem (Rodgers, 2000) and is described in details in J. Navarro and Aythami (2016). The calculation of the model spectra and Jacobians is performed with KOPRA, being called in each step of the iteration. The measurement covariance matrix is calculated from the noise-equivalent spectral radiance provided with the NOMAD level 1a data. The regularization matrix is built from Tikhonov-type terms of different orders which can be combined to obtain a custom-tailored regularization for any retrieval problem. RCP uses a Levenberg-Marquardt damping which is forced to be zero in the last iteration. Convergence is reached when the change of the retrieval parameters with respect to the previous iteration is smaller than the expected noise retrieval error. We are using the nominal noise provided which is typically around 2×10^{-3} in transmittance. The principal output are the retrieved parameters, but RCP can also supply diagnostics of the retrieval such as the averaging kernels, the noise error covariance matrix, or the vertical resolution.

We decided to select a regularization profile that deals with the trade-off between very oscillating extinction vertical profile with low value of vertical resolution and a smooth extinction vertical profile with high value of vertical resolution. A typical result of the level 2 product of RCP is the extinction profile for the NOMAD selected orders shown in Figure 1. The retrieved extinctions differ from the usual evaluation using the onion-peeling method, also named Abel's transform method, since with this global fit we have other key parameters as the averaging kernel and the vertical resolution. This is a crucial difference with the earlier works on aerosols using

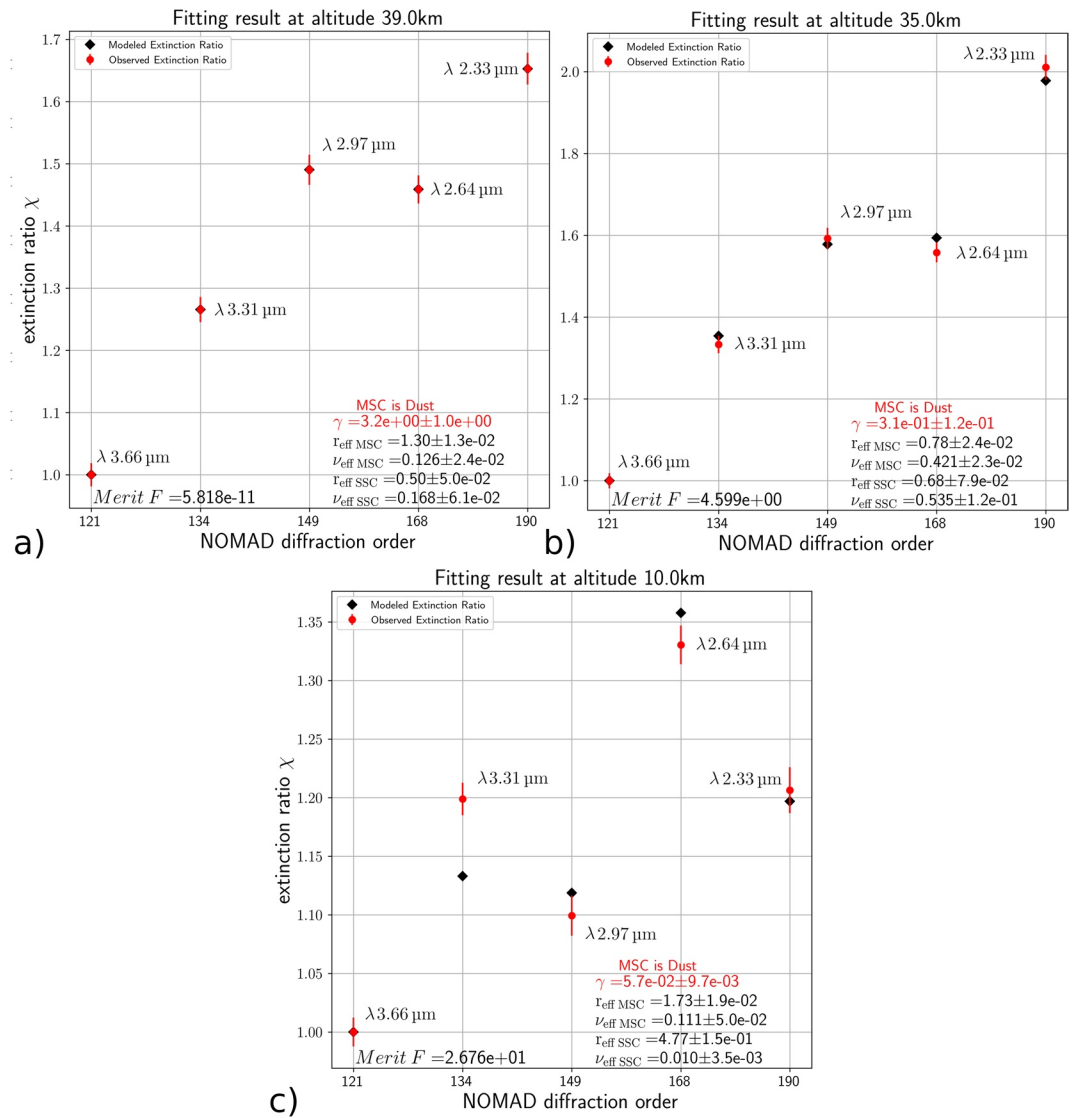


Figure 5. Fitting results example. Red circles represent the extinction ratios evaluated with RCP from NOMAD-SO data. Black diamonds are the modeled extinctions ratios evaluated with the best five parameters, displayed in the bottom right of each panel, retrieved from the fitting procedure.

ACS data (Luginin et al., 2020; Stcherbinine et al., 2020), who used an onion-peeling inversion. We expect our uncertainties to be lower, especially at lower altitudes where errors accumulate with the onion-peeling method.

4. Aerosol Distribution Properties Analysis Scheme

Our method builds on the work carried out by Fedorova et al. (2014) and Luginin et al. (2020) themselves initiated by Montmessin et al. (2002), which focused on assessing Martian aerosol properties from solar occultation and limb observations. We are using the extinction behavior, pre-calculated using Lorenz-Mie theory, over a wide spectral band that is covered by NOMAD with the aim of recovering certain properties of Martian aerosols.

4.1. The Aerosol Size Distribution

The Martian aerosol distributions are modeled using log-normal distributions. The log-normal distribution $n_N(r)$, defined by Equation 2, is the derivative of the aerosol number density N of aerosols with respect to the aerosol radius r . The usual unit of $n_N(r)$ is $\mu\text{m}^{-1} \text{cm}^{-3}$. The log-normal distribution is strictly defined by two parameters,

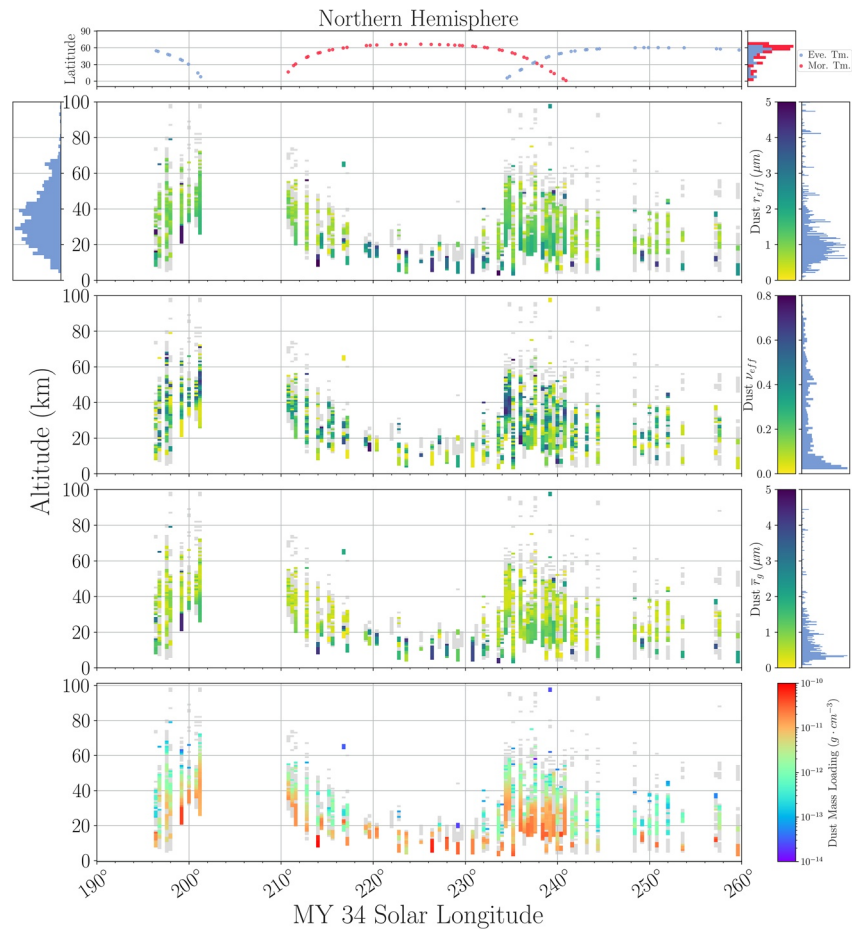


Figure 6. Results of the aerosol distribution properties analysis scheme for dust in the northern hemisphere during the MY34 GDS. The filtered points (high merit function or low/high effective variance) are shown in light gray. All histograms panels are relative occurrences and share the vertical axis with their relevant parameters.

the median radius \bar{r}_g , and the geometric standard deviation σ_g . The median radius is the radius value for which both halves of the population have a below and above the median radius. The geometric standard deviation act in a similar fashion as the standard deviation for the normal distribution with the population in the interval $[\bar{r}_g/\sigma_g; \bar{r}_g \cdot \sigma_g]$ representing 68.2% of the total population.

$$n_N(r) = \frac{dN}{dr} = \frac{N_{\text{tot}}}{\sqrt{2\pi} r \ln(\sigma_g)} \cdot \exp\left(-\frac{(\ln(r) - \ln(\bar{r}_g))^2}{2 \ln(\sigma_g)^2}\right) \quad (2)$$

In the radiative transfer modeling literature, size distributions are generally described using the effective radius r_{eff} and the effective variance ν_{eff} (Hansen & Travis, 1974; Mishchenko et al., 2002; Section 6.3.3.2 in Wolff et al. (2017) which gives a comprehensive overview of particle size distributions used in Martian studies) instead of its usual parameters (i.e., median radius \bar{r}_g and geometric standard deviation σ_g for the log-normal). Indeed, the effective radius and effective variance are parameters with an optical meaning. As the effective radius is the ratio of volume to cross-section, it can be thought of as the ability of a distribution to absorb part of the incident radiation. These two parameters are also used to reformulate the equations essential to radiation transfer theory. We use a log-normal distribution because it is widely used in atmospheric sciences. Its formulation allows us to use values of effective variance greater than 0.5 (Hansen & Travis, 1974). It is also easier to compare our results to previous studies using the same distribution, such as Luginin et al. (2020) and Liuzzi et al. (2020). It is not as straightforward to compare values of effective radius and effective variance from studies using other distributions, such as the Gamma distribution used to study Martian aerosols from CRISM data in Clancy et al. (2019)

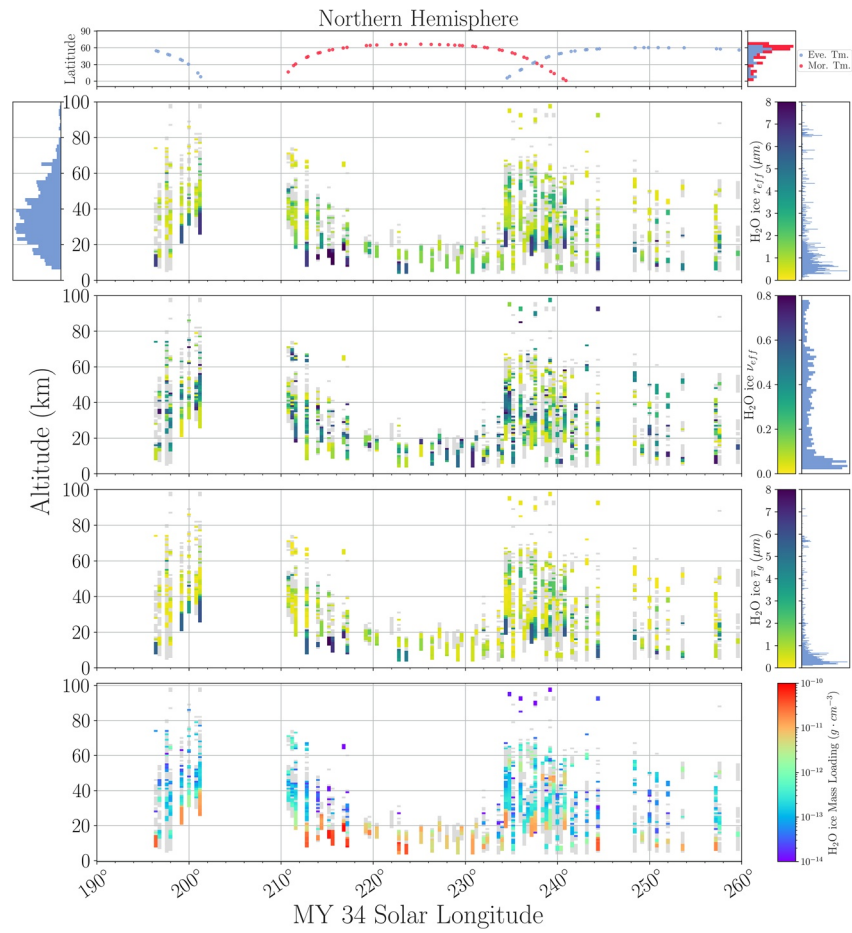


Figure 7. Results of the aerosol distribution properties analysis scheme for H_2O_{ice} in the northern hemisphere during the MY34 GDS. The filtered points (high merit function or low/high effective variance) are shown in light gray. All histograms panels are relative occurrences and share the vertical axis with their relevant parameters.

and from ACS-MIR data in Stcherbinine et al. (2020). For the log-normal distribution, its parameters are related to r_{eff} and ν_{eff} as follow:

$$\sigma_g = \exp\left(\sqrt{\ln(\nu_{eff} + 1)}\right) \quad (3)$$

$$\bar{r}_g = \frac{r_{eff}}{\exp(2.5 \ln^2(\sigma_g))} \quad (4)$$

Figure 2 shows the effect that a variable effective variance has on a log-normal distribution with a fixed effective radius. The value of the effective variance can induce significant biases for any effective radius retrieval, since the observed aerosol distribution may be far removed from the possible distributions available with the selected effective variance. It should also be noted that log-normal by-products, such as mass loading, most numerous radius (mode 0), and any quantities involving log-normal integrals, are strongly affected by the values of each parameter.

For any aerosol size distribution, the extinction k at a wavelength λ is defined as follow:

$$k(\lambda) = N \sigma_{ext}(\lambda, r_{eff}, \nu_{eff}) \quad (5)$$

Where k is the extinction in km^{-1} , N the aerosol number density and $\sigma_{ext}(\lambda)$ is the mean average extinction cross-section at a wavelength λ and for a specific aerosol distribution defined by the two parameters (r_{eff}, ν_{eff}) . To get rid of the number density N , we can construct a new variable χ defined as follow:

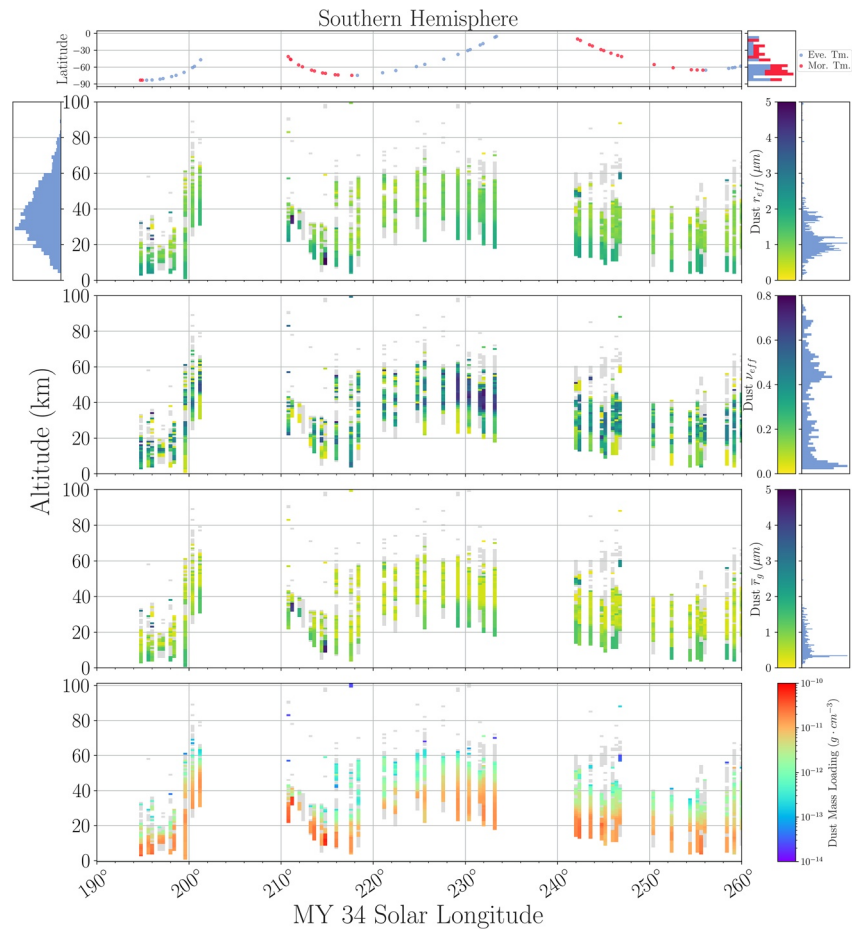


Figure 8. Results of the aerosol distribution properties analysis scheme for dust in the southern hemisphere during the MY34 GDS. The filtered points (high merit function or low/high effective variance) are shown in light gray. All histograms panels are relative occurrences and share the vertical axis with their relevant parameters.

$$\chi(\lambda) = \frac{k(\lambda)}{k(\lambda_0)} \quad (6)$$

On Mars, the aerosol distribution shows a bimodal behavior as shown by Fedorova et al. (2014). To model this characteristic of Martian aerosol, we define an extinction ratio χ_m (Equation 7) for a mixture of dust and water ice as done in Luginin et al. (2020). In Equation 7, the subscript d is for dust and wi is for water ice. The term γ is the ratio of the number densities of water ice over dust, N_{wi}/N_d .

$$\chi_m(\lambda) = \frac{k_d(\lambda) + \gamma k_{wi}(\lambda)}{k_d(\lambda_0) + \gamma k_{wi}(\lambda_0)} \quad (7)$$

4.2. Evaluation of the Extinction Ratio Using a Lorenz-Mie Code

To calculate the average extinction cross-section of a given aerosol distribution, we need the refractive indices of the aerosols. For Dust, we use data from Wolff et al. (2009), with an effective radius between 0.05 and 5 μm and an effective variance between 0.001 and 0.8. For water ice, we must also take into account the temperature dependence of refractive indices. We use data from Warren and Brandt (2008) and Clapp et al. (1995) to construct a set of refractive indices values for water ice ranging from 100 to 270 K with 1 K step. We interpolate between the available values to build refractive indices at unavailable temperatures. The effective radius of water

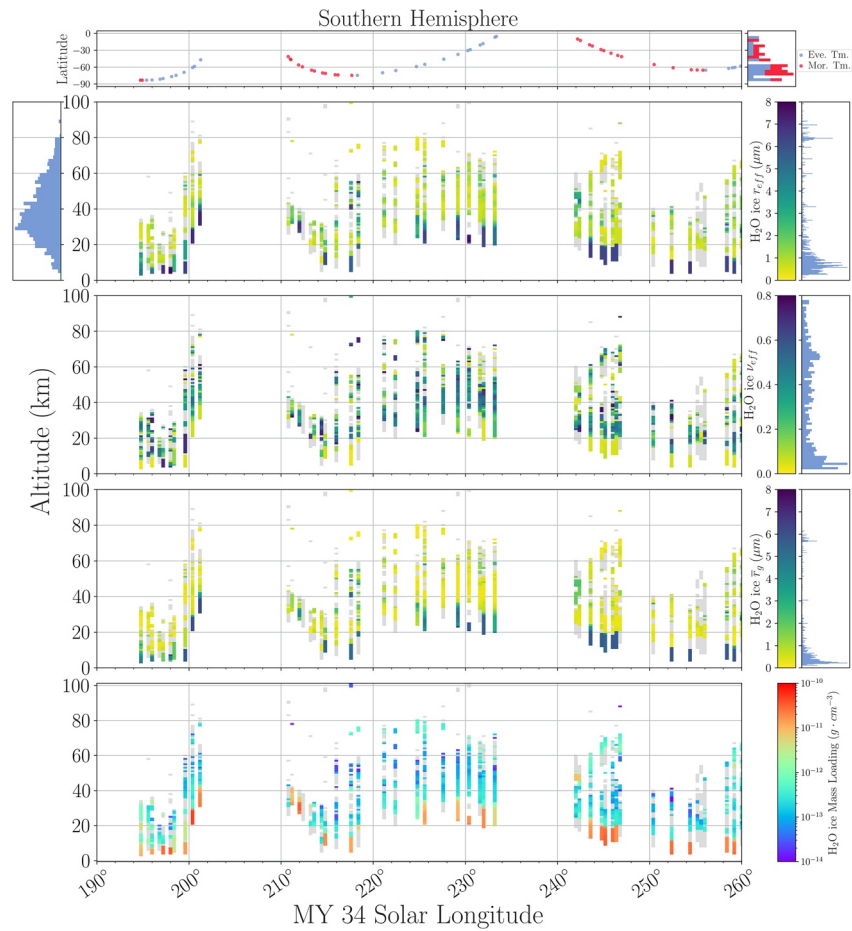


Figure 9. Results of the aerosol distribution properties analysis scheme for H_2O_{ice} in the southern hemisphere during the MY34 GDS. The filtered points (high merit function or low/high effective variance) are shown in light gray. All histograms panels are relative occurrences and share the vertical axis with their relevant parameters.

ice ranges from 0.05 to 10 μm and the effective variance from 0.01 to 0.8. We extended the range of effective variance down to low values to test the robustness of our fitting procedure. An effective variance of 0.001 translates into a geometric standard deviation of 1.03, which is close to a monodisperse distribution. A monodisperse aerosol distribution is unrealistic, hence extremely low values of ν_{eff} . Nonetheless, a value of $\nu_{eff} = 0.01$ corresponds to $\sigma_g = 1.10$, which is still a narrow distribution but quite far from a monodisperse one. An exceptionally low effective variance, below 0.01, will allow us to filter the results of the fitting procedure to detect unrealistic results, even when other the other retrieved parameters would be considered good.

Using the evaluated refractive indexes, we run a Lorenz-Mie code for polydisperse spherical particle taken from Mishchenko et al. (2002) for a set of (r_{eff}, ν_{eff}) to evaluate the mean average extinction cross-section at the wavelengths of the selected NOMAD order (cf., Table 1).

Figures 3 and 4 show the broadband behavior of the extinction ratio χ with ν_{eff} in the NOMAD spectral range for different values of the effective radius. Our refractive index interpolation method is entirely similar to that used in Luginin et al. (2020). NOMAD-SO's IR spectral range allows us to probe an aerosol population within a specific size and number density window. Nevertheless, readers should be aware that such a window does not represent all particles sizes present on Mars. Figure 13 gives an idea of the possible population to be recovered using our method. For example, we can see particles with an effective radius greater than 2 μm but only with number densities less than 1 cm^{-3} . This does not mean that a denser population of the same size does not exist on Mars, only that it is too opaque for NOMAD-SO. The same reasoning can be applied to a population of smaller particles. A high particle density is required to obtain a significant drop in transmittance. A less dense population

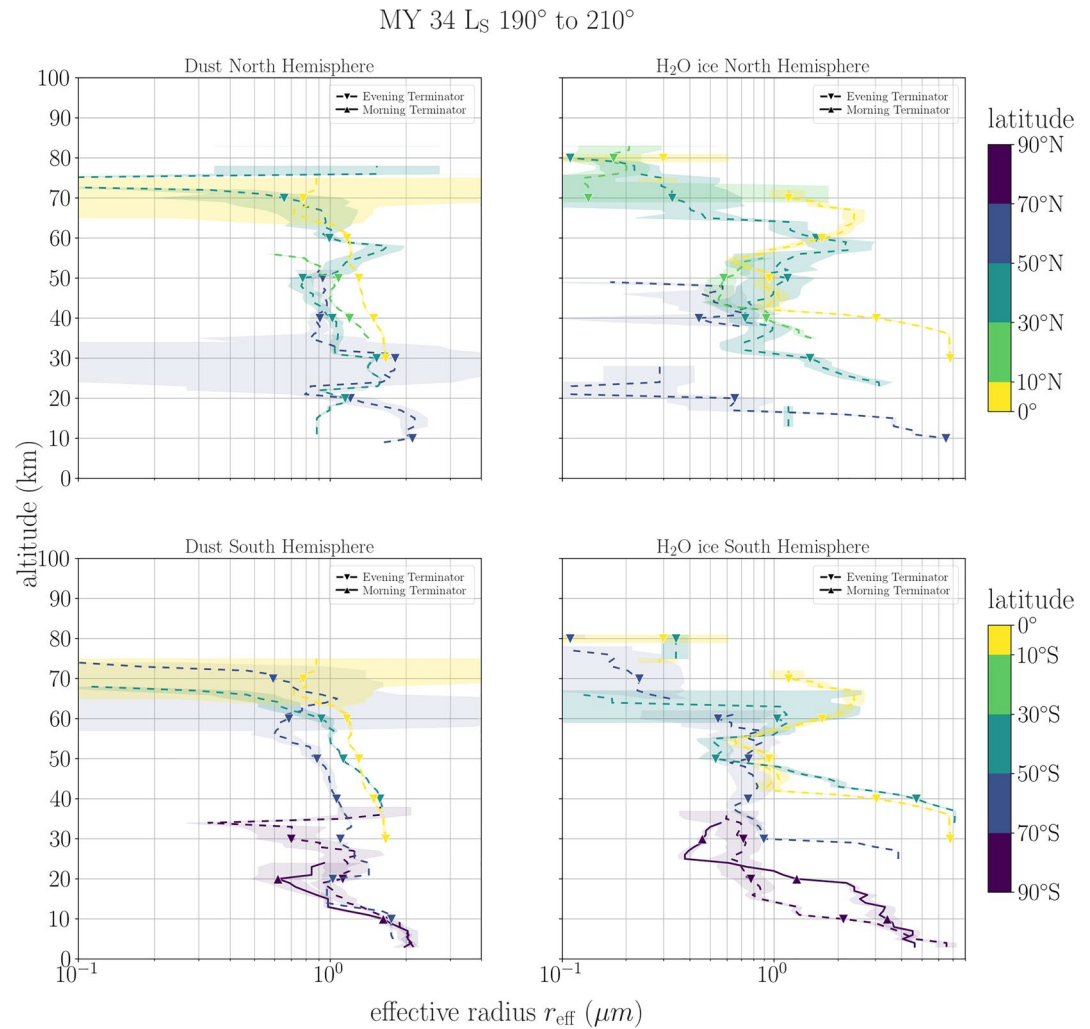


Figure 10. Vertical profiles of the effective radius during the GDS at five latitude ranges. The vertical profiles are derived from a vertical running average using a vertical window of 10 km. The error displayed by the colored area is the greatest value between the standard deviation of the data points and the error in the mean from the running average.

may exist, but is transparent to NOMAD-SO. Furthermore, Figures 3 and 4 show that a weaker gradient between populations with high effective variance than that between populations with lower effective variance. This effect is greatest for particle populations with larger effective radii. This generally translates into larger errors on the effective variance, but also explains the low percentage of successful fits of 35% (see Paper II, Section 2.2).

4.3. The Fitting Procedure

The reasoning behind our fitting procedure is similar to that presented in Luginin et al. (2020). To evaluate the best set of parameters (r_{eff} , ν_{eff} , γ) that describe the distribution of Martian aerosols at a given altitude, we find the minimum of a merit function that is the residual between a forward modeling of the extinction ratios and the extinctions ratios retrieved from the NOMAD-SO transmittance data. We define the unbiased residual as:

$$R = \sqrt{\frac{1}{M - p} \left(\frac{\chi_m - \chi_{\text{obs}}}{\delta_{\text{obs}}} \right)} \quad (8)$$

Where M is the total number of points, p is the degrees of freedom, χ_m is the modeled extinction ratio, χ_{obs} is the retrieved extinction ratio from NOMAD observations and δ_{obs} is its associated error. Finding the minimum of R^2 gives us the standard least-square problem.

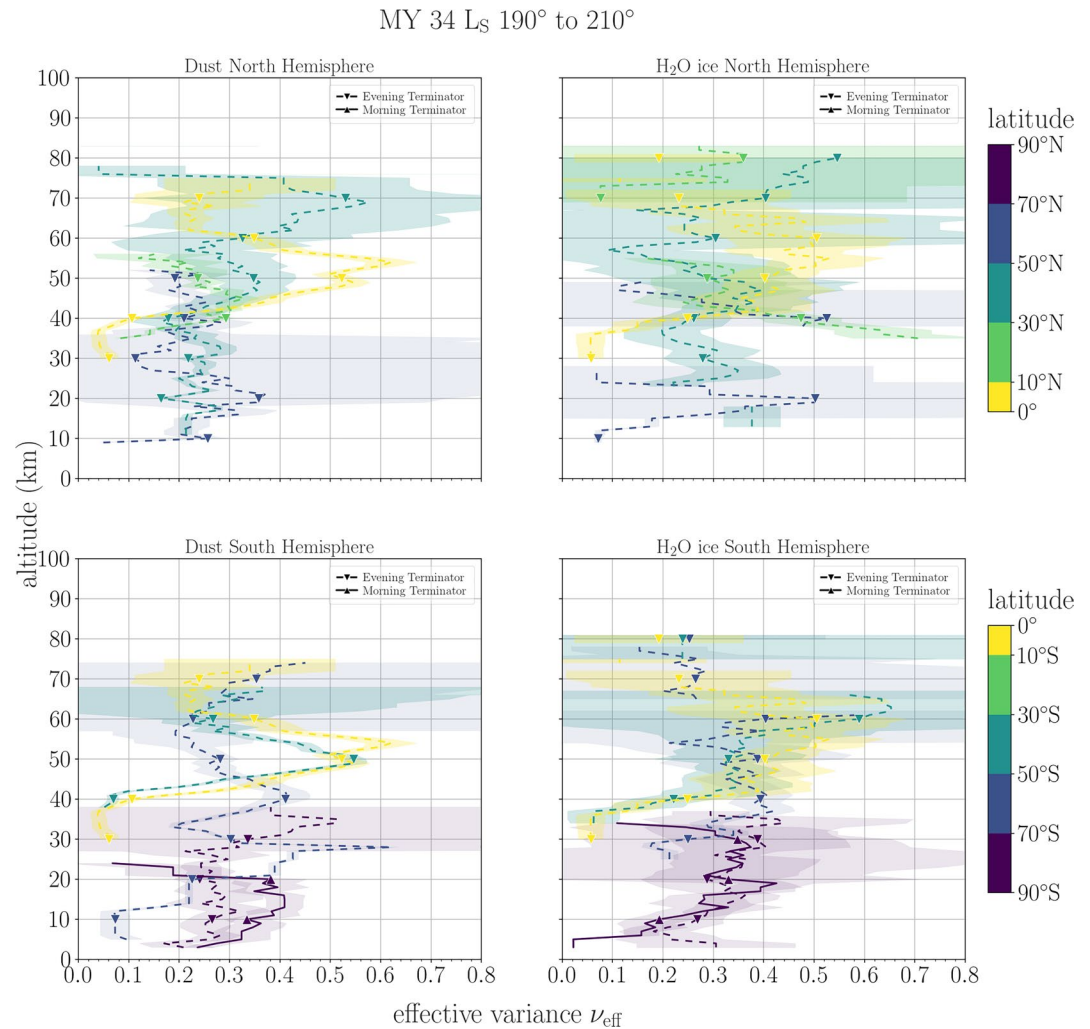


Figure 11. Vertical profiles of the effective variance during the GDS at five latitude ranges. The vertical profiles are derived from a vertical running average using a vertical window of 10 km. The error displayed by the colored area is the greatest value between the standard deviation of the data points and the error in the mean from the running average.

We use a mixture of non-linear least square algorithm (referred as NLSQ hereafter) and brute force algorithm to evaluate the best set of parameters ($r_{\text{eff}}, \nu_{\text{eff}}, \gamma$) for pure dust, pure water ice and a mixture of the two represented by γ . The NLSQ algorithm is provided by the SciPy v 1.10.1 Python package (Virtanen et al., 2020). We have chosen the dogbox algorithm as our solver. This is a Trust Region algorithm (Branch et al., 1999; Sorensen, 1982) but considers rectangular trust regions as opposed to conventionally used ellipsoids (Voglis & Lagaris, 2019). The minimization problem is solved using the dogleg method (Powell, 1970).

Our fitting procedure follows these steps at each altitude point:

1. Filtering the extinction vertical profiles for altitudes with an averaging kernel diagonal component <0.03 and/or if an extinction is lower than $1 \times 10^{-5} \text{ km}^{-1}$ for any wavelength. This minimal value of $1 \times 10^{-5} \text{ km}^{-1}$ is equal of that used in Luginin et al. (2020). This is a safe value, given NOMAD-SO's measurement noise. Below this threshold, the extinction profile generally begins to oscillate around 0.
2. Using a NLSQ algorithm to find the best ($r_{\text{eff}}, \nu_{\text{eff}}$) for pure Dust
3. Using a NLSQ algorithm to find the best ($r_{\text{eff}}, \nu_{\text{eff}}$) for pure H₂O ice
4. The best fitting component (i.e., the lowest Merit Function value) between pure dust and H₂O ice is set as Main Spectral Component (MSC), the other as Secondary Spectral Component (SSC)
5. Using brute force over γ for two nested NLSQ algorithm that find the best set of parameters ($r_{\text{MSC eff}}, \nu_{\text{MSC eff}}, r_{\text{SSC eff}}, \nu_{\text{SSC eff}}, \gamma$).

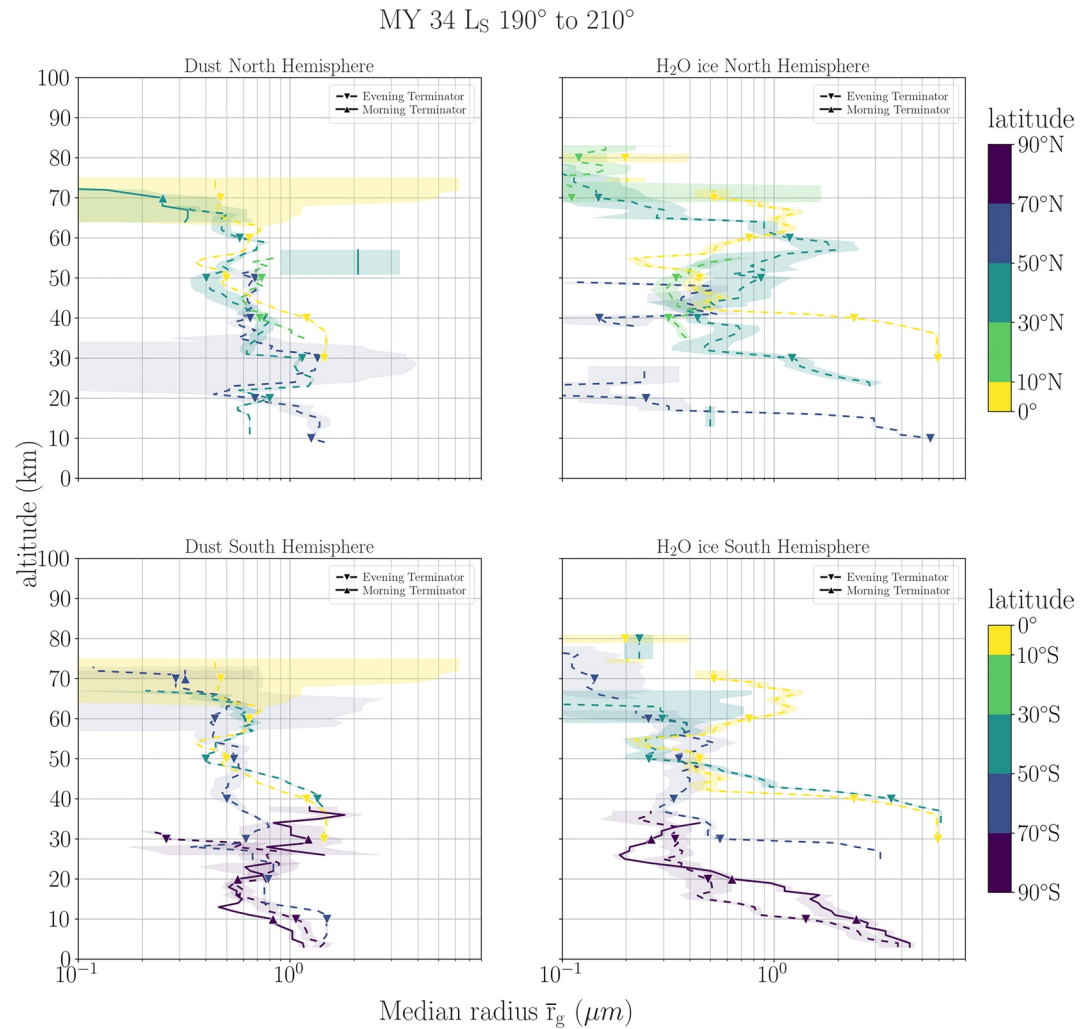


Figure 12. Vertical profiles of the median radius during the GDS at five latitude ranges. The vertical profiles are derived from a vertical running average using a vertical window of 10 km. The error displayed by the colored area is the greatest value between the standard deviation of the data points and the error in the mean from the running average.

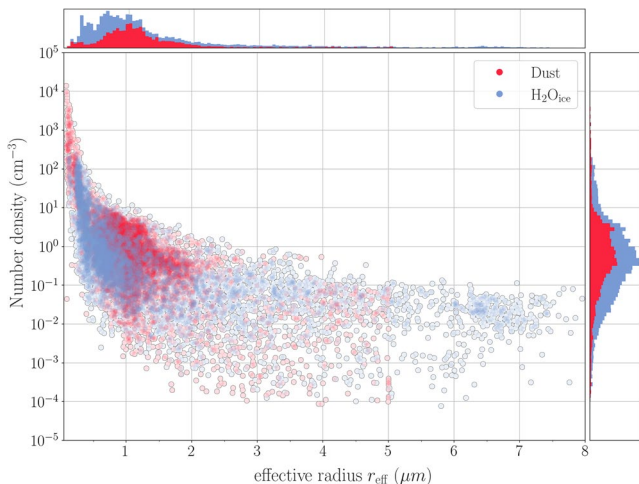


Figure 13. Number density against effective radius for our entire data set, MY 34 L_S 180° to MY 35 L_S 180°.

- (a) Selection of the set of parameters with the lowest Merit Function value during Brute Force.
- (b) Evaluation of the ν_{eff} error with retrieving r_{eff} alongside ν_{eff} for MSC and SSC using NLSQ algorithm. The other three parameters are considered fixed. The errors are evaluated from the diagonal component of the covariance matrix.
- (c) Evaluation of $r_{\text{MSC eff}}$, $r_{\text{SSC eff}}$ and γ using NLSQ algorithm. The $\nu_{\text{MSC eff}}$ and $\nu_{\text{SSC eff}}$ are fixed from the previous step. The errors are evaluated from the diagonal component of the covariance matrix.
6. The Number densities of Dust (Equation 9a) and water ice (Equation 9b) are evaluated using the retrieved extinctions from inversion of NOMAD data with RCP and the evaluated mean average extinction cross-section from the Lorentz-Mie code. The mass loading is rigorously evaluated using the third order moment of the log-normal. The density of mineral dust is set at $\mu_{\text{Dust}} = 2.5 \text{ g cm}^{-3}$ and the density of water ice to $\mu_{\text{H}_2\text{O ice}} = 0.9 \text{ g cm}^{-3}$. These are standard values for densities, used in Luginin et al. (2020) and Liuzzi et al. (2020). The errors are evaluated using common propagation errors formulas.

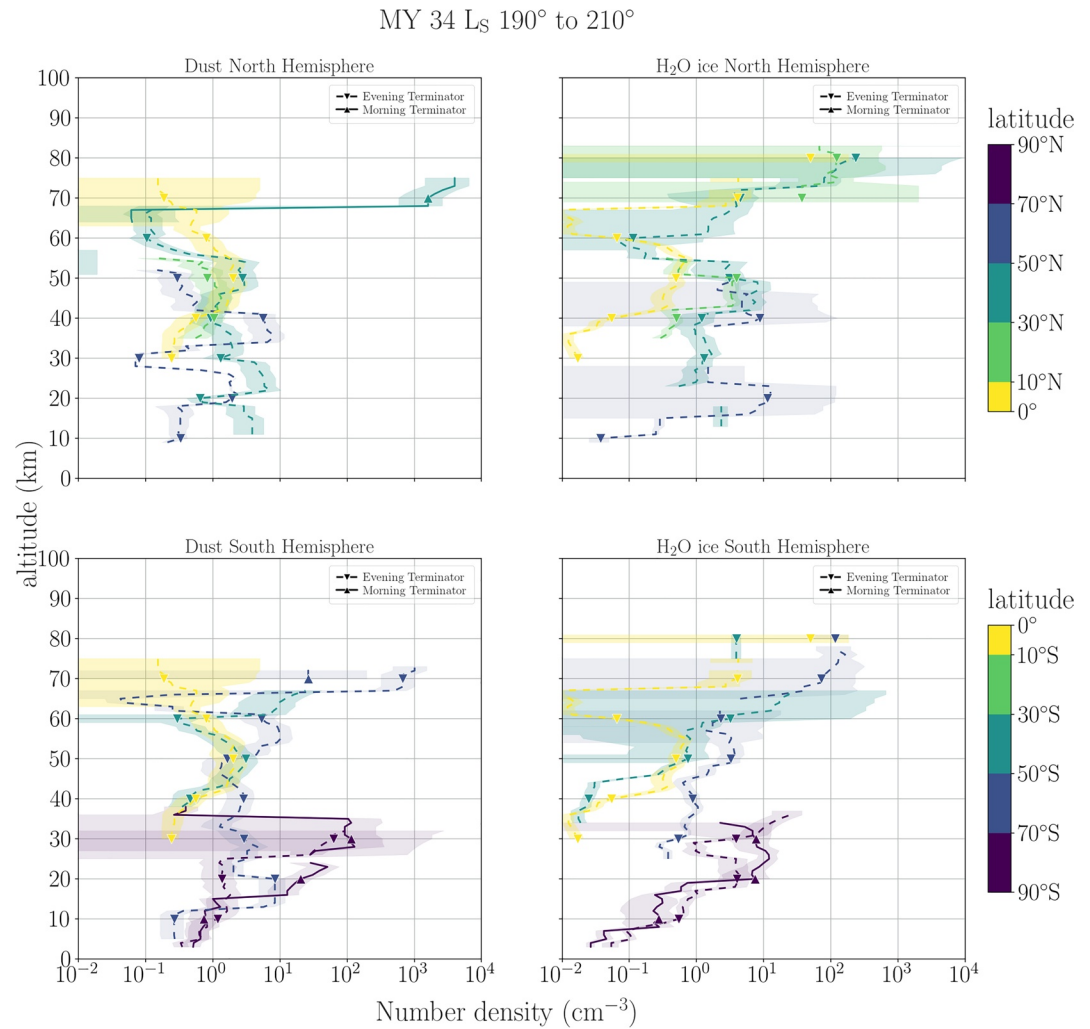


Figure 14. Vertical profiles of the number density during the GDS at five latitude ranges. The vertical profiles are derived from a vertical running average using a vertical window of 10 km. The error displayed by the colored area is the greatest value between the standard deviation of the data points and the error in the mean from the running average.

$$N_d = \frac{1}{M} \sum_{i=1}^M \frac{k(\lambda_i)}{((\sigma_d(\lambda_i) + \gamma \sigma_{wi}(\lambda_i)))} \quad (9a)$$

$$N_{wi} = \frac{1}{M} \sum_{i=1}^M \frac{k(\lambda_i)}{(\gamma^{-1} \sigma_d(\lambda_i) + \sigma_{wi}(\lambda_i))} \quad (9b)$$

Parameters errors are calculated from the diagonal component of the covariance matrix provided by the NLSQ algorithm. Figure 5 panel (a) is an example of a good fit result (all output parameters of the fitting procedure are shown) while panel (b) represent a result of acceptable fit and panel (c) a result rejected due to poor fit (high merit function value). We empirically selected a goodness-of-fit threshold value of 5 for the Merit Function. We also exclude every result where the effective variance is below 0.02 or above 0.78 to be sure that even with a merit function below 5, the evaluated effective variance does not come close to the limit of the model, which cannot be considered a robust result. Additionally, we also filter our results when the vertical resolution is greater than a given value, which we set at 8 km. This value reflects results with low information content,

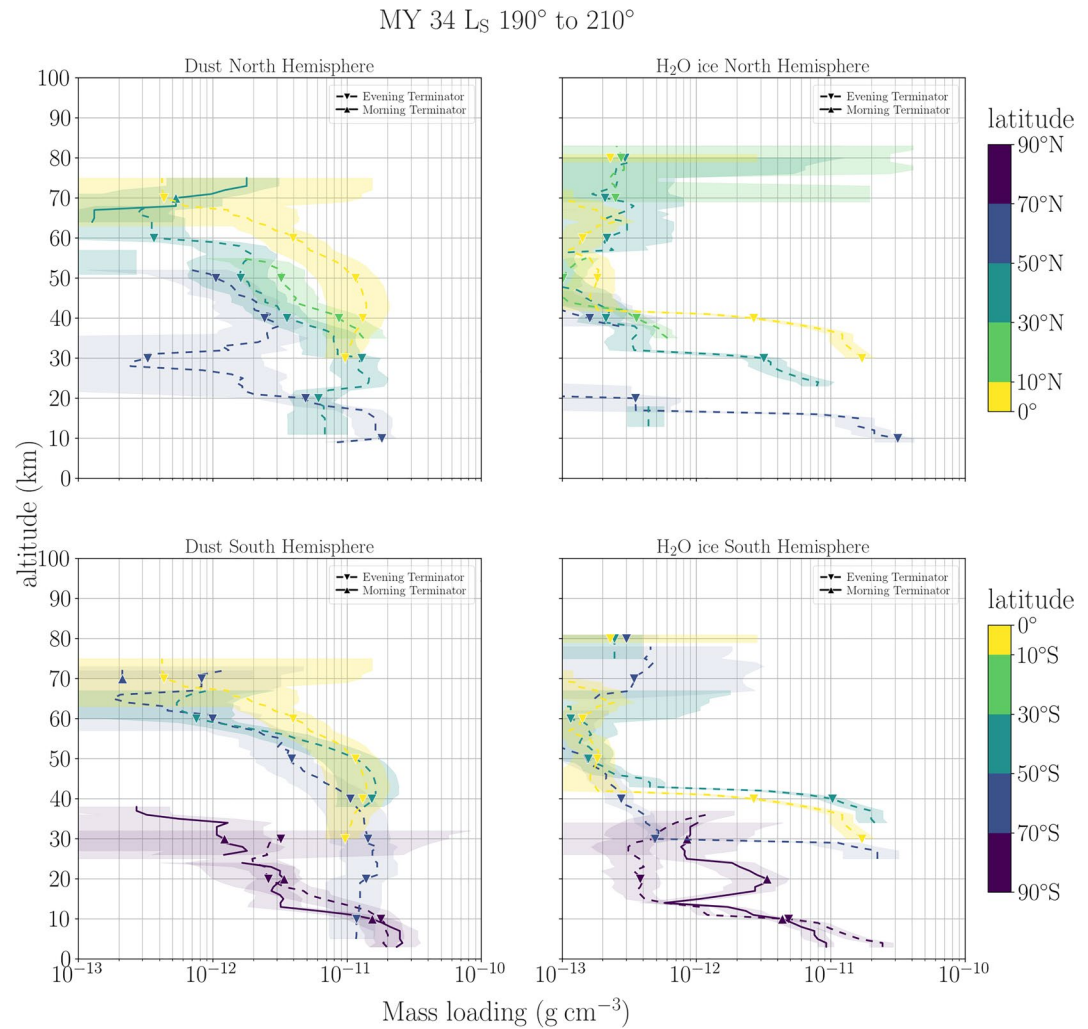


Figure 15. Vertical profiles of the mass loading during the GDS at five latitude ranges. The vertical profiles are derived from a vertical running average using a vertical window of 10 km. The error displayed by the colored area is the greatest value between the standard deviation of the data points and the error in the mean from the running average.

such as opaque layers with low averaging kernel but still greater than our threshold value of 0.03, which deviates from the actual vertical sampling of the instrument, which is a few hundred meters. This means that if the retrieval process requires information from more than 8 data points to produce one extinction value, we consider it unreliable. This value of 8 km is also close the Martian atmospheric scale height which gives a good idea of how the atmosphere changes with altitude. This is not a minimum height of the vertical structure of aerosols, which we know can extend more than 10 km high, but a threshold of reliability of the robustness and quality of our results.

5. Results and Discussion

5.1. Peak of the MY 34 GDS, L_S 190° to L_S 210°

As reported in Section 1, two regional dust storms merged into a GDS at $L_S \sim 195^\circ$ during MY 34. In both hemispheres, we detected dust and water ice aerosols reaching altitudes of up to 90 km (see Figures 6–9).

Our NOMAD data set starts at $L_S \sim 194^\circ$ and ends at $L_S \sim 202^\circ$. Unfortunately, during this period we do not cover the northern polar regions ($>70^\circ\text{N}$). Figures 10–12 show the vertical profiles and latitudinal variation

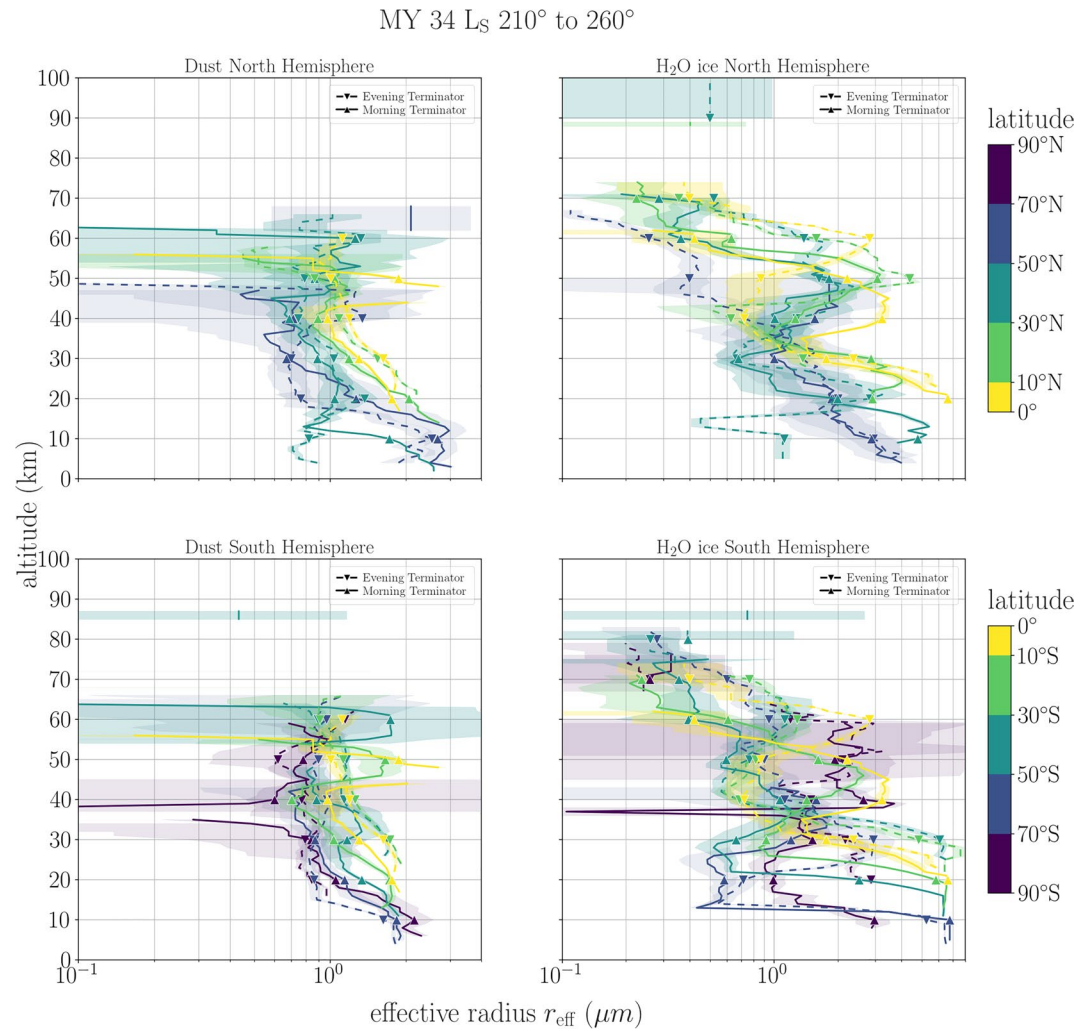


Figure 16. Vertical profiles of the effective radius during the GDS decay at five latitude ranges. The vertical profiles are derived from a vertical running average using a vertical window of 10 km. The error displayed by the colored area is the greatest value between the standard deviation of the data points and the error in the mean from the running average.

of aerosol distribution parameters for the MY 34 GDS peak. High southern latitudes, $>60^\circ$, are imaged until $L_S \sim 200^\circ$ while observed northern latitudes are mainly for mid-latitudes (30° – 60°) until $L_S 202^\circ$. TGO observations resumed after the onset the GDS, which developed from the northern regional storm in Acidalia Planitia (Sánchez-Lavega et al., 2019; Shirley et al., 2020). The GDS has spread further in the southern hemisphere than in the northern hemisphere (Kass et al., 2020; Smith, 2019). This is reflected in Figures 10–12 where southern high latitude panels show a higher altitude of lowermost aerosol detection, ~ 40 km, than their northern counterparts as previously observed by Luginin et al. (2020), Stcherbinine et al. (2020), and Liuzzi et al. (2020). Overall, during the GDS, cloud top altitude reached 60 km with some aerosol detection up to 80 km. Cloud top altitudes show no north-south pattern up to latitudes $\sim 60^\circ$. Above 60° , the northern hemisphere is less affected by the GDS, and its top cloud altitude is lower than that of its southern counterpart. Vertical profiles at equatorial and southern mid-latitudes show the increase in aerosol content during the GDS peak of MY 34 (Kass et al., 2020; Smith, 2019). Since we only cover the evening terminator during the MY 34 GDS, with the exception of a few orbits in the southern polar region which is less affected by the GDS, we cannot conclude about a diurnal behavior of the aerosol parameters we evaluated during the MY 34 GDS.

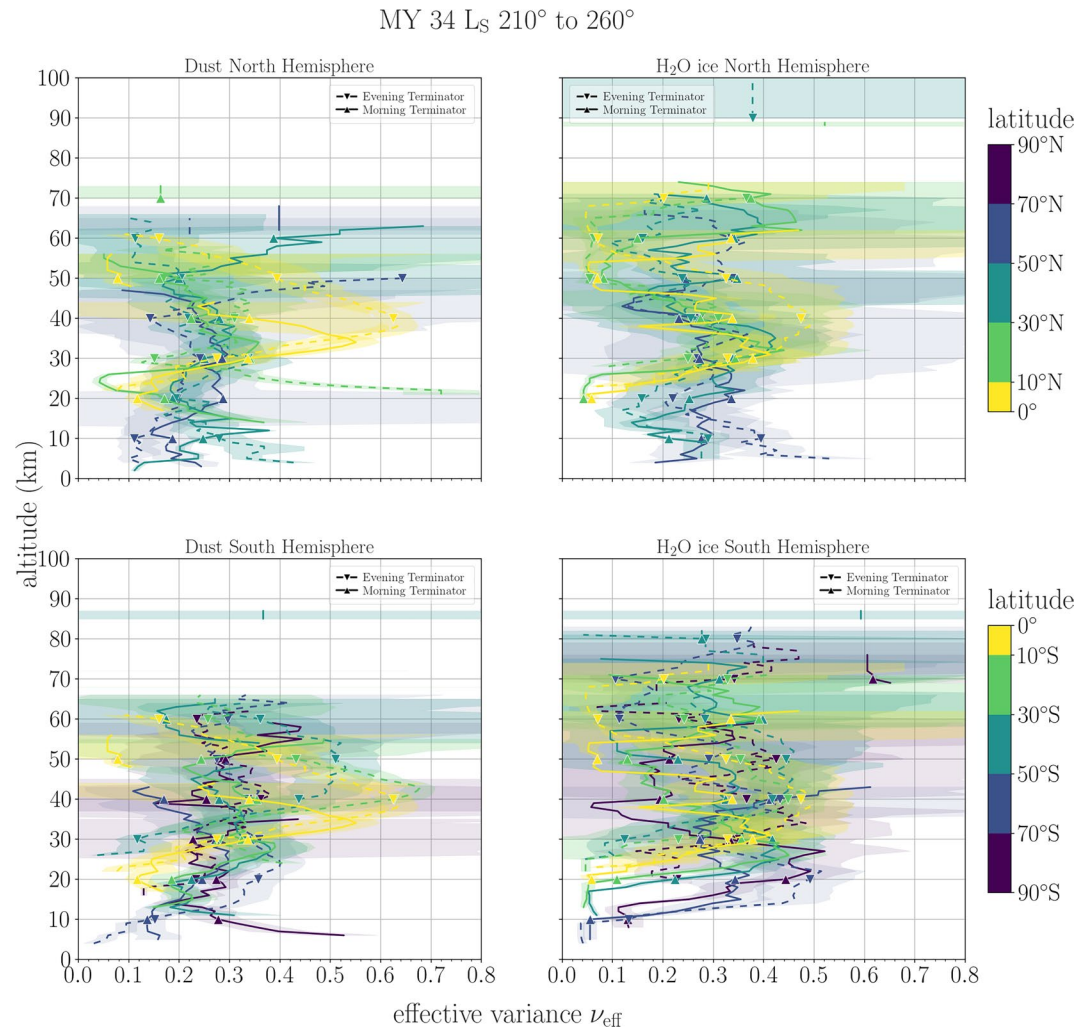


Figure 17. Vertical profiles of the effective variance during the GDS decay at five latitude ranges. The vertical profiles are derived from a vertical running average using a vertical window of 10 km. The error displayed by the colored area is the greatest value between the standard deviation of the data points and the error in the mean from the running average.

Top altitude of aerosol detection: The top altitude of aerosol detection is simply the highest altitude at which we have a robust aerosol detection. This means that we have extinction greater than $1 \times 10^{-5} \text{ km}^{-1}$ at wavelengths of all our selected orders of NOMAD-SO. This leads to a successful retrieval of aerosol parameters (effective radius and variance). We have a lower water ice top altitude of aerosol detection during the peak of the GDS (L_S 194°– L_S 202°) in both hemispheres (see Figures 7 and 9) compared with ACS (Luginin et al., 2020; Stcherbinine et al., 2020) and previous results using NOMAD-SO (Liuzzi et al., 2020). For example, in the northern hemisphere, the detection of water ice aerosols from ACS and NOMAD-SO data can go up to 100 km whereas we mainly reach ~ 70 km with a few occurrences of water ice aerosols at ~ 80 km. The difference with Liuzzi et al. (2020), which also uses NOMAD-SO, could stem from a few differences between our analyses. First, Liuzzi et al. (2020) used any combination of the 5 diffraction order available, which leads to a larger subset of NOMAD-SO data and may better cover the high-altitude water ice haze present in the mesosphere. Our fixed choice of 5 orders limits the number of orbits available. We have tried to maximize the spectral range and always include orders 121 and 190 (from 3.66 to 2.3 μm). Second, we use a minimum value of $1 \times 10^{-5} \text{ km}^{-1}$ for extinction, whereas Liuzzi et al. (2020) has no lower limit in extinction. During the peak of the GDS and roughly above 80 km, water ice extinction can approach but remains below $1 \times 10^{-5} \text{ km}^{-1}$ which is our cut-off value. A more in-depth comparison between our two NOMAD teams would be necessary to study the consequences of these differences. An exhaustive comparison of the ACS extinction vertical profiles and our extinction vertical profiles could also shed light on these discrepancies.

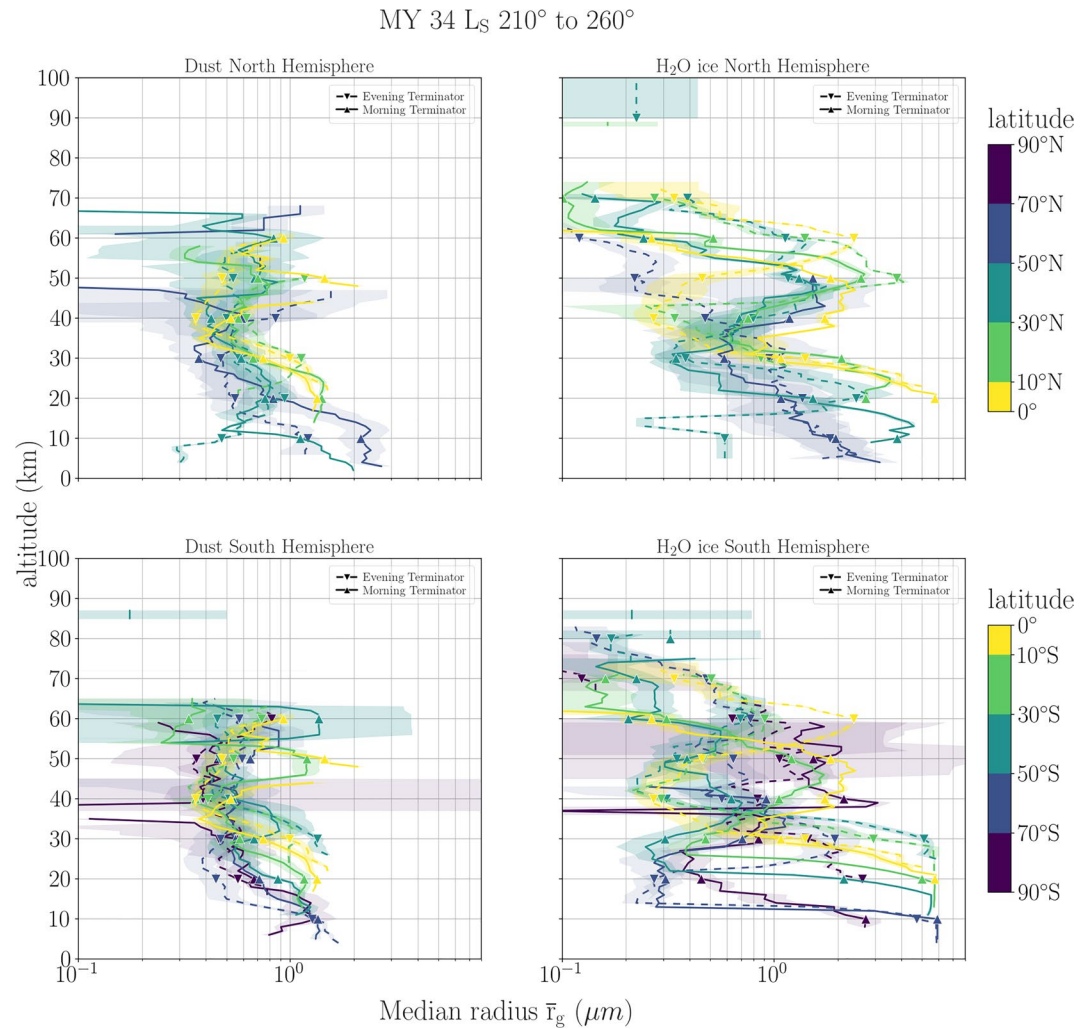


Figure 18. Vertical profiles of the median radius during the GDS decay at five latitude ranges. The vertical profiles are derived from a vertical running average using a vertical window of 10 km. The error displayed by the colored area is the greatest value between the standard deviation of the data points and the error in the mean from the running average.

Vertical behavior of dust and water ice effective radius: Dust r_{eff} is generally close to $1 \mu\text{m}$ while water ice r_{eff} tends to be sub-micron (Figure 10). As the lower layers are mainly opaque in the IR due to the high aerosol content, we may simply not have access to altitudes where effective size of water ice could be on average larger than its dust counterpart. This particular scenario occurs near the polar regions where we probe altitudes of down to 5 km (Figure 10). Here, the effective size of water ice is larger than of dust, and both are larger than $1 \mu\text{m}$. In general, our effective dust and water ice sizes decrease with altitude, in agreement with previous observations from CRISM (Clancy et al., 2019; Guzewich & Smith, 2019) and ACS (Luginin et al., 2020; Stcherbinine et al., 2020). During large-scale dust events, the effective aerosol size in the altitude range of 30–60 km should be almost constant and close to the effective size of the lower layers (Clancy et al., 2010). This is also the case in our NOMAD-SO results for dust aerosols. These do not show a significant gradient with altitude. However, our effective water ice size shows a steeper vertical gradient, decreasing from about $1 \mu\text{m}$ at 40 km to sub-micron values in just a few kilometers, which is consistent with ACS results (Luginin et al., 2020; Stcherbinine et al., 2020). Another interesting result of our data is that the vertical structure of water ice aerosols is different from that of dust. While the effective size of dust seems to decrease linearly with altitude (Figure 10), water ice has a more complicated structure. We can identify four layers (Figure 10), the lowest containing water ice of effective size $>3 \mu\text{m}$, a second layer containing sub-microns water ice particles, a third layer with a increase of water ice effective size of around $1\text{--}2 \mu\text{m}$, and finally an upper layer which is dominated by a sharp decrease in effective water ice effective radius down to sub-microns values.

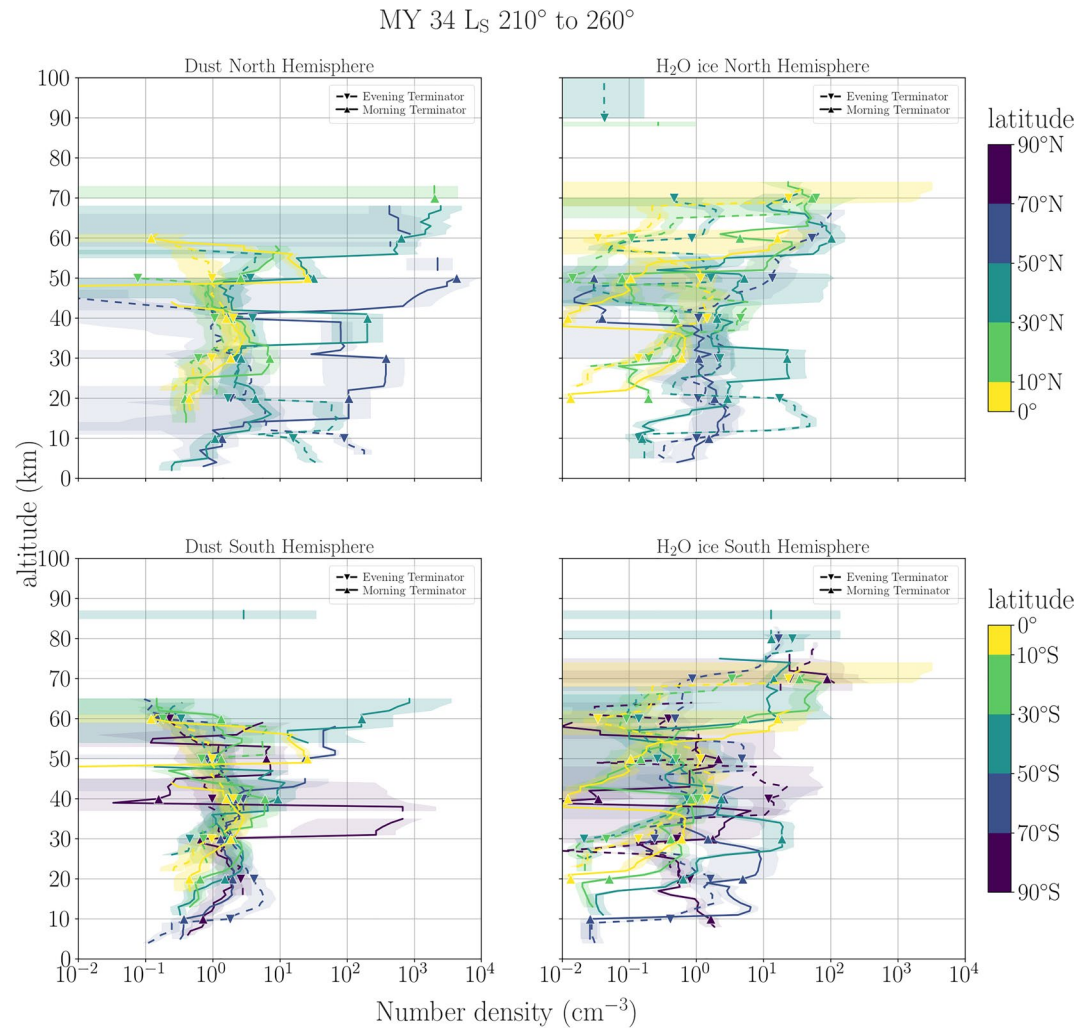


Figure 19. Vertical profiles of the number density during the GDS decay at five latitude ranges. The vertical profiles are derived from a vertical running average using a vertical window of 10 km. The error displayed by the colored area is the greatest value between the standard deviation of the data points and the error in the mean from the running average.

Comparison of the effective radius values: As indicated above, water ice particles show a greater vertical gradient between the lower (<40–60 km depending on the latitude) and upper (>40–60 km depending on the latitude) layers. For the lower layers, we find an effective radius of around 1–2 μm for latitudes affected by the GDS. This effective size decreases toward values between 0.1 and 0.3 μm within ~ 10 km. These values are consistent with the results of Stcherbinine et al. (2020) using ACS MIR data and Liuzzi et al. (2020) using NOMAD-SO data. Luginin et al. (2020), using ACS-TIRVIM data, finds effective radius closer to 2 μm in the lower layers but with a similar gradient leading to an effective radius close to 0.1 μm in the upper layers. The effective dust size remains close to 1 μm and between 0.5 and 0.8 μm for water ice, which is in good agreement with TES results (Clancy et al., 2010), while our retrieved effective dust size close to 1 μm is lower than the value between 1.5 and 2 μm reported in Clancy et al. (2010).

The aerosol effective variance during the peak of the MY 34 GDS: The effective variance, ν_{eff} , is a parameter fixed in most Martian aerosols studies to date (Guzewich & Smith, 2019; Liuzzi et al., 2020; Smith et al., 2013; Stcherbinine et al., 2020; Wolff et al., 2009). Typical values are assumed to be between 0.1 and 0.4 for dust and water ice aerosols. This is a generally acceptable assumption as extinction is mainly affected by the effective aerosol size (see Figures 3 and 4 and discussions in Wolff and Clancy (2003) and Wolff et al. (2006)). Following the work of Fedorova et al. (2014) and Luginin et al. (2016, 2020), we have included the ν_{eff} as a free parameter in our fitting procedure (described in Section 4.3). We also provide an uncertainty associated with the evaluation of

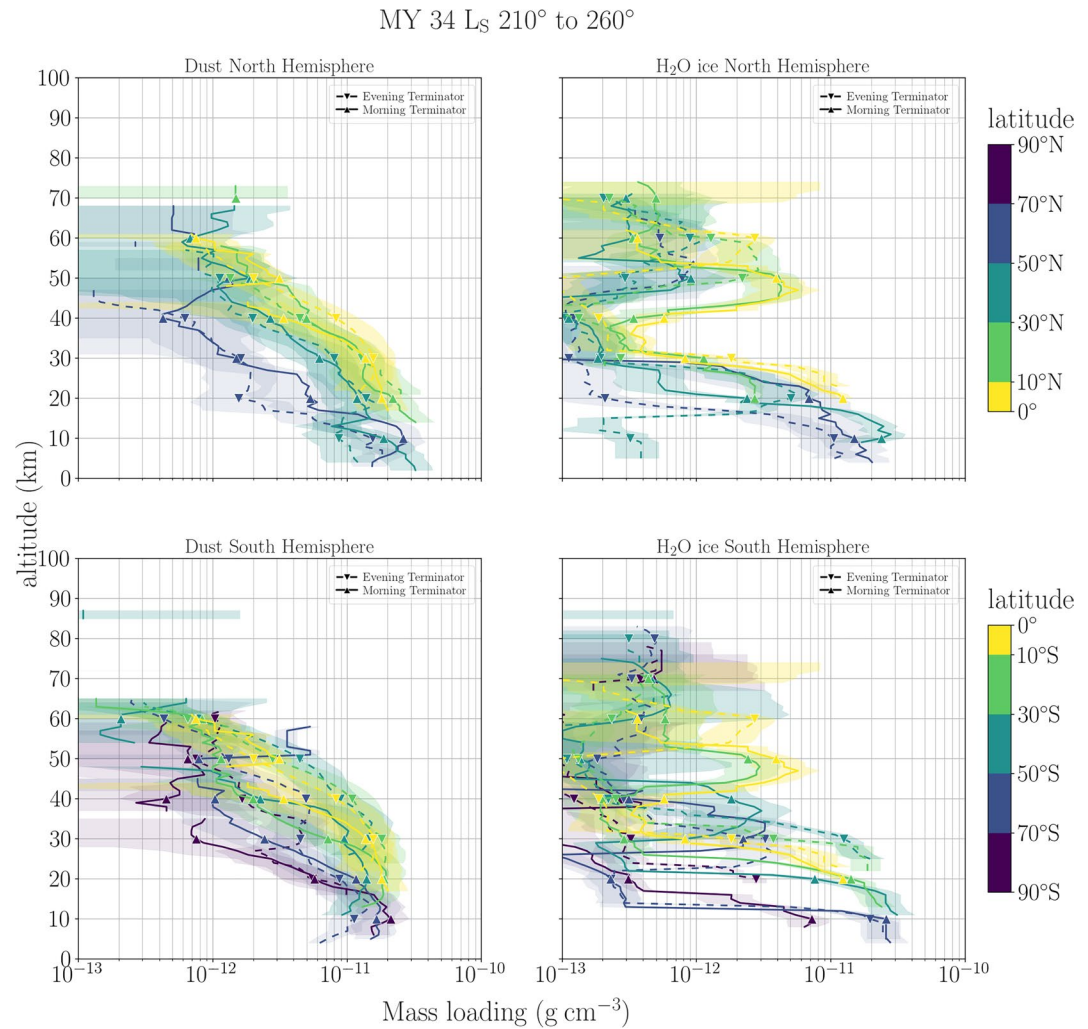


Figure 20. Vertical profiles of the mass loading during the GDS decay at five latitude ranges. The vertical profiles are derived from a vertical running average using a vertical window of 10 km. The error displayed by the colored area is the greatest value between the standard deviation of the data points and the error in the mean from the running average.

ν_{eff} , which is a step forward from previous work. Figure 11 shows that the errors can be exceptionally large, in line with its effect on extinction leading to higher uncertainty during the fitting procedure. As Luginin et al. (2020), we find that lower effective variances (<0.2) are more numerous (see Figures 6–9) with a sharp increase toward the lowest values. The effective variance shows no behavior as a function of altitude, but does exhibit a North/South asymmetry. Dust effective variance in the southern hemisphere shows a greater number of occurrences in the 0.4–0.6 interval (Figure 8) than in the northern hemisphere (Figure 6). This is also the case for water ice even if the increase is less pronounced (Figures 7 and 9). This increase is present throughout the GDS, and also during its decay. This increased aerosol population with ν_{eff} 0.4–0.6 in the southern hemisphere, and in the northern one also, is not observed during the first half of MY 35 as described in Paper II.

The aerosol median radius during the peak of the MY 34 GDS. The median radius, \bar{r}_g , is a physical characteristic often overlooked when talking about aerosol “size.” The literature (see Kahre et al. (2017) and Wolff et al. (2017) and references therein) prefers to use the effective radius, r_{eff} , as an indicator of the aerosol “size.” This is a common practice (a habitual simplification) in atmospheric science. However, as we developed in Section 4.1, the effective radius is not representative of a real “size” because it is a ratio of moments of the size distribution and this changes significantly according to the value of its effective variance (Figure 2). In contrast, the value of the median radius does not change with a vary with the geometric standard deviation (see Section 4.1), which explains why it is a more robust indicator of aerosol “size” in case of the log-normal distribution. Nevertheless,

in most studies of Martian aerosols, the effective variance is fixed and the effective radius is therefore linked to a single size distribution. Consequently, in these cases, the effective radius can be safely used to describe aerosol particle size. Furthermore, although \bar{r}_g can be evaluated analytically for the log-normal distribution, this is not the case for the Gamma or modified Gamma distribution. As we have chosen to the effective variance, we can also present our results for the median radius. These results during the GDS are presented in Figure 12. The specific population of dust aerosols with a median radius of $\sim 0.3 \mu\text{m}$ (see Paper II for detailed figure), which can be almost constant for a few kilometers of altitude, is not visible on the mean vertical profiles. The dust median radius does not show the same vertical gradient as that observed for the effective radius.

Our evaluation of the effective variance applied to the calculation of the median radius affects the vertical profile of dust size by almost suppressing entirely the slight vertical gradient of the effective radius. Dust, for each specific range of latitudes, shows a vertical structure similar to that of water ice, with a set of distinct layers located at similar altitudes (Figure 12). The median radius of water ice is generally smaller than that of dust, with values below $0.5 \mu\text{m}$. The largest water ice particles can reach $\sim 5 \mu\text{m}$ and are observed at altitudes below 20 km in the southern polar region (see Figure 12) where aerosol opacity is low enough to allow sounding at such low altitudes (Kass et al., 2020; Smith, 2019). At lower latitudes, where the effect of the GDS on aerosol opacity is more pronounced ($\sim 50^\circ\text{N}$ to $\sim 70^\circ\text{S}$ in Smith (2019) and Kass et al. (2020)), water ice particles of $\sim 1 \mu\text{m}$ can be observed alongside dust particles of the same size, at around 40 km.

The aerosol number density during the peak of the MY 34 GDS: Aerosol number density, in cm^{-3} , is related to the full set of evaluated parameters ($\gamma, \nu_{d \text{ eff}}, \nu_{wi \text{ eff}}, r_{d \text{ eff}}, r_{wi \text{ eff}}$) (see Section 4.3). During the GDS of MY 34, the number density of dust and water ice was mainly in the range 0.1 to 10 cm^{-3} , in agreement with the ACS results of Luginin et al. (2020) for the same period, with few occurrences above and below this range (Figure 14). Aerosol number density over the GDS period follows a similar trend to that shown for the effective radius in Figure 13. On average, the larger the particle, the lower the number density.

The aerosol mass loading during the peak of the MY 34 GDS: The mass loading, in g cm^{-3} shown in Figure 15, starts uniformly $\sim 1 \times 10^{-11} \text{ g cm}^{-3}$ for each latitude range. The lowermost aerosol detection altitude differs according to the latitudes affected or not by the GDS. For example, the southern polar region (see Figure 15 panel 70°S – 90°S) has a mass loading $\sim 1 \times 10^{-11} \text{ g cm}^{-3}$ around 10 km while the equator (see Figure 15 panel 10°N – 10°S) has a mass loading $\sim 1 \times 10^{-11} \text{ g cm}^{-3}$ but at much higher altitude, close to 40 km. An increase in aerosol content can be clearly observed by studying the mass loading during the GDS of MY 34. In an interval of about 10–20 km, the dust mass loading decreases by about one order of magnitude, down to $\sim 10^{-12} \text{ g cm}^{-3}$. Water ice shows a similar decrease, but with a steeper vertical gradient than dust and remains in the range from 10^{-13} to $10^{-12} \text{ g cm}^{-3}$. Our results are in good agreement with Luginin et al. (2020).

5.2. Decay of the MY 34 GDS, $L_S 210^\circ$ to $L_S 260^\circ$

Time trends of the aerosol parameters during the MY 34 GDS decay phase: During the GDS decay phase, the lowermost altitude of aerosol detection decreases with time. In the northern hemisphere (Figures 6 and 7), for latitudes $\sim 30^\circ$ and the same time of day, the lowermost altitude of aerosol detection decreases from ~ 30 km just after the peak of the GDS ($L_S 215^\circ$) to ~ 15 km at $L_S 238^\circ$. For the southern hemisphere (Figures 8 and 9) and for latitudes around 60° at the morning terminator, the lowermost altitude of aerosol detection decreases from ~ 30 km at $L_S 215^\circ$ to ~ 5 km at $L_S 255^\circ$. Comparing Figures 10 and 16, we find no noticeable change in typical values of effective dust size between the peak of the GDS and the GDS decay phase. However, water ice aerosols show an increase in effective size in the aerosol upper layers. In Figure 16, the equatorial band is populated by water ice aerosols with an effective size of $\sim 2 \mu\text{m}$ in the upper layers (40–50 km for the morning terminator and ~ 60 km for the evening terminator) compared with the $\sim 1 \mu\text{m}$ found during the GDS peak at an equivalent latitude (Figure 10). Dust also shows the same slight vertical decrease in effective size during the GDS decay phase as during the GDS peak. Water ice still shows a similar vertical structure during the GDS peak and its decay phase, with lower layers of an effective size $> 3 \mu\text{m}$, intermediate layers of sub-microns effective particles and upper layers of around 1 – $2 \mu\text{m}$ effective sizes with a decrease toward sub-micron sizes during the last few kilometers. This increase in effective size of water ice, previously reported by Liuzzi et al. (2020) with NOMAD-SO and also observed in ACS data (Luginin et al., 2020; Stcherbinine et al., 2020), may be associated with the decrease in temperature, with the intensity of the GDS decreasing at the same time. Liuzzi et al. (2020) also postulates

that a regional “rocket” dust storm occurring at $L_S \sim 230^\circ$ in equatorial and northern mid-latitudes could help explain the increase in the effective size of dust and water ice simultaneously. Figures 6–9 show that NOMAD-SO observations cover latitudes $<30^\circ\text{N}$ at $L_S 234^\circ$ and coincide with the vertical profiles of more abundant aerosol content. In the northern hemisphere, from $L_S 216^\circ$ to $L_S 243^\circ$, NOMAD-SO mainly observes the northern hemisphere at latitudes close to 60°N where the GDS has not extended much, resulting vertical profiles with lower aerosol content (Figures 6 and 7). Moreover, data starting at $L_S 234^\circ$ from evening terminator observations correspond to higher aerosol content, until latitudes of the morning and evening terminator cross at $L_S \sim 238^\circ$. We find it difficult to distinguish a dust event as geographically small as a “rocket” dust storm from the GDS, and particularly at a location and time when the GDS can still be considered somewhat active. We argue that the increase of effective size of water ice in the upper aerosol layers is mainly due to a decrease in atmospheric air temperature during the GDS decay phase. The period from $L_S 230^\circ$ – 240° in the equatorial to northern mid-latitude region is no exception, since the same hypothesis about the drop in air temperature due to the declining GDS intensity can explain the same behavior of effective water ice size for the later period from $L_S 240^\circ$ to 260° . This increase in the effective size of water ice during the decay phase is reflected in the mass loading. By comparing the mass loading during the GDS peak (Figure 15) and during the GDS decay phase (Figure 20), we find that the mass loading of the upper water ice layers increases by at least one order of magnitude from a mass loading $<1 \times 10^{-13} \text{ g cm}^{-3}$ to $\sim 3 \times 10^{-12} \text{ g cm}^{-3}$ for northern to southern mid-latitudes. The lower layers have approximately the same mass loading of water ice with maximum values around $1 \times 10^{-11} \text{ g cm}^{-3}$. The mass loading of dust does not show the same increase as that of water ice, and maintains a similar value during the peak and decay phases of the GDS, rising from $\sim 1 \times 10^{-11} \text{ g cm}^{-3}$ in the lower layers to $\sim 1 \times 10^{-12} \text{ g cm}^{-3}$ in the upper layers. What affects dust mass loading the most is the decrease in altitude of the aerosol content during the GDS decay phase. For example, in the equatorial region, Figures 15 and 20 show that the vertical dust profile extends approximately from 30 to 70 km during the GDS peak and 20–60 km during the decay phase.

Aerosol diurnal and latitudinal behavior during the MY 34 GDS decay phase: As described in Barnes et al. (2017), non Sun-synchronous observations of Mars such as TGO can provide valuable insight on diurnal radiative forcing in Mars' atmosphere. The GDS decay phase is long enough for us to have morning and evening NOMAD-SO observations at equivalent latitudes. We find a clear diurnal behavior in the effective size of water ice aerosols (Figure 16). For latitudes, whether north or south, below 70° , the vertical profiles of the effective size at the evening terminator are more extended in altitude than the vertical profiles at the morning terminator. This difference in vertical extension is particularly marked in the equatorial region, where upper layers of water ice are located between 40 and 50 km at the morning terminator and up to 60 km at the evening terminator. Interestingly, the lower layers of water ice remain at similar altitudes, just under 30 km, at both the morning and evening terminator. For mid-latitudes, the same behavior can be observed but at different altitudes. Nevertheless, the effective size of water ice shows a North-South asymmetry. At northern latitudes between 10° and 50° , the upper layers (40–60 km) have an effective water ice size in the range between 2 and 4 μm , while in the south, the effective size in the upper layers remains close to 1 μm . These diurnal and latitudinal variations in the effective size of water ice are reflected in the median radius (Figure 18). The increase in water ice size follows that of its effective size, and is not offset by a change in its effective variance. In addition, the size gradient from the middle (~ 20 – 50 km) to upper (~ 40 – 70 km) layers at the equator and mid-latitudes is more pronounced for the median radius of water ice, with values ranging from 0.3 to 0.4 μm , while its effective size is more in the order of 0.6–1.0 μm in the middle layers. This diurnal and latitudinal vertical difference in water ice aerosol size is an indirect indication of the effect of the GDS on the vertical temperature profile. The combination of the effect of the GDS effect on the radiative forcing expected to enhance meridional transport of water vapor at higher latitudes (Neary et al., 2020) and the diurnal thermal tides producing a higher diurnal temperature gradient in the northern hemisphere during the northern autumn (Lee et al., 2009) explains the vertical structure of water ice size and the promotion of larger water ice aerosols in the northern hemisphere and at higher altitude at the evening terminator. Equivalent results and explanation were given by Liuzzi et al. (2020). The vertical behavior of the water ice mass loading (Figure 20) is strongly correlated with the size of the water ice aerosol. This means that there is no radical change in the vertical profile of aerosol number density between the GDS peak (Figure 14) and its decay phase (Figure 19), nor in the effective variance (Figures 11 and 17), with the exception of the maximum altitude of the aerosol content, which decreases with the GDS intensity. The increase in water ice size and mass loading is therefore primarily due to atmospheric condition favoring water ice formation. In other words, lower air temperature and higher water vapor content. Dust size does not exhibit the same diurnal and latitudinal behavior as water ice. We note that the vertical profiles of dust size are fairly similar in morning and evening terminator observations (Figures 16

and 18). Nevertheless, we can observe slight differences in the vertical dust size profiles between the morning and evening terminator, with evening dust size profiles extending higher than the morning profiles. For example, in the southern hemisphere (Figure 16) at mid-latitudes 10°S to 30°S, vertical profiles of dust size start at 15 km at the morning terminator and 25 km at the evening terminator with a similar effective size of about 1.8 μm . But, looking at Figure 8, we note that these observations are taken at a difference in L_s of $\sim 10^\circ$ one from the other. This temporal delay in these observations, as the intensity of the GDS decreases could explain the differences between dust vertical profiles at the morning and evening terminator. It could therefore be the effect of the GDS decay, of a decrease in the upper extent of the aerosol content, and not an actual diurnal variability. The L_s delay from one observation to the next cannot explain the greater diurnal behavior of water ice size in the upper layers described above.

6. Conclusion

The NOMAD-SO channel (Vandaele et al., 2015) is a solar occultation infrared spectrometer onboard ExoMars TGO working in the 2.2–4.3 μm spectral range (2,200 to 4,500 cm^{-1}). In this work we exploit the NOMAD-SO's spectral range, by selecting and combining five of its diffraction orders, to obtain vertical profiles of key aerosol properties, including extinction, particle sizes and variance, and the nature of aerosol particles. We use vertical profiles of calibrated transmittance from level 1 data provided by the PI team. These level 1 scans are pre-processed by an in-house algorithm developed to clean the data of any spectral shifts and/or continuum curvature. To retrieve the extinction vertical profile due to aerosol we use a state-of-the-art line by line radiative transfer forward model code called KOPRA, in conjunction with the iterative non-linear inversion scheme RCP, designed and developed at the Institute of Meteorology and Climate Research (IMK) of Karlsruhe Institute for Technology and previously used in J. Navarro and Aythami (2016). A priori and first guess profiles of the atmospheric thermal structure and composition, required by RCP, are taken from specific runs of the Mars PCM (Forget et al., 1999) carried out at the IAA.

We have developed a fitting procedure based on a mixing of brute force and non-linear least-square methods. This allows us to evaluate the aerosol distribution's parameter for pure dust, water ice or a mixture of both. Our results cover the first Martian year of NOMAD-SO science operation, including the GDS of MY 34 (the focus of this article) but also the MY 34 C-Storm, the early dust event of MY 35 and the first half of MY 35, presented in Paper II.

This study takes place following the methodology of earlier works by Luginin et al. (2020), using ACS-TIRVIM, of Stcherbinine et al. (2020) using ACS-MIR and of Liuzzi et al. (2020) using NOMAD-SO data for MY 34. Our study focuses on the general trend in aerosol distribution and composition over a full Martian year. We have added to this method the evaluation of the effective variance with altitude, latitude, and season, alongside the more usual effective radius. We show that the effective variance adopts a broad set of values and is largely represented by values < 0.2 , and that a slight *N/S* asymmetry occurred during the GDS of MY 34. Water ice particles are predominantly $< 0.5 \mu\text{m}$ with micron-sized particles typically found in the lower layers of aerosol content or in specific upper layers during the MY 34 GDS decay phase. The bimodal distribution of dust effective radius, 1 and 1.8 μm , results in a median radius close to 1 μm with a notable peak at 0.3 μm . Overall, our results concerning the MY 34 GDS are in good agreement with established knowledge and in particular with the results of ACS (Luginin et al., 2020; Stcherbinine et al., 2020) and NOMAD-SO (Liuzzi et al., 2020).

This study, and Paper II, represent the first step at the IAA to evaluate the Martian aerosol composition and distribution using NOMAD-SO data. We plan to study in more details the available data (our 5-orders selection represents roughly 55% of the data set used by Liuzzi et al. (2020) for MY 34), the one presented in this general study but also NOMAD-SO data for the end of MY35 and start of MY36.

Data Availability Statement

The results data from our inversion of NOMAD-SO data (extinction profiles) and aerosol fitting procedure, r_{eff} , ν_{eff} , γ and their derivatives, are being archived and available from [Dataset] Stolzenbach (2023).

Acknowledgments

Authors Aurélien Stolzenbach, Miguel-Angel López Valverde, Adrian Brines, Ashimananda Modak, Bernd Funke and Francisco González-Galindo acknowledges financial support from the Severo Ochoa Grant CEX2021-001131-S funded by MCIN/AEI/10.13039/501100011033. F. González-Galindo is funded by the Spanish Ministerio de Ciencia, Innovación y Universidades, the Agencia Estatal de Investigación and EC FEDER funds under project RTI2018-100920-J-100. B. Funke also acknowledges support by project PID2019-110689Rb-100/AEI/10.13039/501100011033. ExoMars is a space mission of the European Space Agency (ESA) and Roscosmos. The NOMAD experiment is led by the Royal Belgian Institute for Space Aeronomy (IASB-BIRA), assisted by Co-PI teams from Spain (IAA-CSIC), Italy (INAF-IAPS), and the United Kingdom (Open University). This project acknowledges funding by the Belgian Science Policy Office (BELSPO), with the financial and contractual coordination by the ESA Prodex Office (PEA 4000103401, 4000121493) as well as by UK Space Agency through Grants ST/V002295/1, ST/V005332/1, and ST/S00145X/1 and Italian Space Agency through Grant 2018-2-PH.0. This work was supported by the Belgian Fonds de la Recherche Scientifique—FNRS under Grant 30442502 (ET_HOME). This project has received funding from the European Union's Horizon 2020 research and innovation program under Grant agreement No 101004052 (RoadMap project). US investigators were supported by the National Aeronautics and Space Administration. We want to thank the LMD/IPSL and LATMOS/IPSL teams for the continuous development of the Mars PCM. We would like to thank the two anonymous reviewers whose detailed comments on the structure and scientific content of this article were of great help to us.

References

Barnes, J. R., Haberle, R. M., Wilson, R. J., Lewis, S. R., Murphy, J. R., & Read, P. L. (2017). The global circulation. In F. Forget, M. D. Smith, R. T. Clancy, R. W. Zurek, & R. M. Haberle (Eds.), *The atmosphere and climate of Mars* (pp. 229–294). Cambridge University Press. <https://doi.org/10.1017/9781139060172.009>

Bertrand, T., Wilson, R. J., Kahre, M. A., Urata, R., & Kling, A. (2020). Simulation of the 2018 global dust storm on Mars using the NASA Ames Mars GCM: A multitracer approach. *Journal of Geophysical Research: Planets*, *125*(7), e2019JE006122. <https://doi.org/10.1029/2019JE006122>

Branch, M. A., Coleman, T. F., & Li, Y. (1999). A subspace, interior, and conjugate gradient method for large-scale bound-constrained minimization problems. *SIAM Journal on Scientific Computing*, *21*(1), 1–23. <https://doi.org/10.1137/S1064827595289108>

Brines, A., López-Valverde, M., Stolzenbach, A., Modak, A., Funke, B., Galindo, F., et al. (2022). Water vapor vertical distribution on Mars during perihelion season of MY 34 and MY 35 with ExoMars-TGO/NOMAD observations. *Journal of Geophysical Research: Planets*, e2022JE007273. <https://doi.org/10.1029/2022je007273>

Chassefière, E., Blamont, J. E., Krasnopolsky, V. A., Korablev, O. I., Atreya, S. K., & West, R. A. (1992). Vertical structure and size distributions of Martian aerosols from solar occultation measurements. *Icarus*, *97*(1), 46–69. [https://doi.org/10.1016/0019-1035\(92\)90056-D](https://doi.org/10.1016/0019-1035(92)90056-D)

Clancy, R. T., Montmessin, F., Benson, J., Daerden, F., Colaprete, A., & Wolff, M. J. (2017). Mars clouds. In F. Forget, M. D. Smith, R. T. Clancy, R. W. Zurek, & R. M. Haberle (Eds.), *The atmosphere and climate of Mars* (pp. 76–105). Cambridge University Press. <https://doi.org/10.1017/9781139060172.005>

Clancy, R. T., Sandor, B. J., Wolff, M. J., Christensen, P. R., Smith, M. D., Pearl, J. C., et al. (2000). An intercomparison of ground-based millimeter, MGS TES, and Viking atmospheric temperature measurements: Seasonal and interannual variability of temperatures and dust loading in the global Mars atmosphere. *Journal of Geophysical Research*, *105*(E4), 9553–9571. <https://doi.org/10.1029/1999JE001089>

Clancy, R. T., Wolff, M. J., & Christensen, P. R. (2003). Mars aerosol studies with the MGS TES emission phase function observations: Optical depths, particle sizes, and ice cloud types versus latitude and solar longitude. *Journal of Geophysical Research*, *108*(E9), 5098. <https://doi.org/10.1029/2003JE002058>

Clancy, R. T., Wolff, M. J., Smith, M. D., Kleinböhl, A., Cantor, B. A., Murchie, S. L., et al. (2019). The distribution, composition, and particle properties of Mars mesospheric aerosols: An analysis of CRISM visible/near-IR limb spectra with context from near-coincident MCS and MARCI observations. *Icarus*, *328*, 246–273. <https://doi.org/10.1016/j.icarus.2019.03.025>

Clancy, R. T., Wolff, M. J., Whitney, B. A., Cantor, B. A., Smith, M. D., & McConnochie, T. H. (2010). Extension of atmospheric dust loading to high altitudes during the 2001 Mars dust storm: MGS TES limb observations. *Icarus*, *207*(1), 98–109. <https://doi.org/10.1016/j.icarus.2009.10.011>

Clapp, M. L., Worsnop, D. R., & Miller, R. E. (1995). Frequency-dependent optical constants of water ice obtained directly from aerosol extinction spectra. *The Journal of Physical Chemistry*, *99*(17), 6317–6326. <https://doi.org/10.1021/j100017a010>

Colaprete, A., Barnes, J. R., Haberle, R. M., Hollingsworth, J. L., Kieffer, H. H., & Titus, T. N. (2005). Albedo of the south pole on Mars determined by topographic forcing of atmosphere dynamics. *Nature*, *435*(7039), 184–188. <https://doi.org/10.1038/nature03561>

Davies, D. W. (1979). Effects of dust on the heating of Mars' surface and atmosphere. *Journal of Geophysical Research*, *84*(B14), 8289–8293. <https://doi.org/10.1029/JB084iB14p08289>

Fedorova, A. A., Korablev, O. I., Bertaux, J. L., Rodin, A. V., Montmessin, F., Belyaev, D. A., & Reberac, A. (2009). Solar infrared occultation observations by SPICAM experiment on Mars-Express: Simultaneous measurements of the vertical distributions of H₂O, CO₂ and aerosol. *Icarus*, *200*(1), 96–117. <https://doi.org/10.1016/j.icarus.2008.11.006>

Fedorova, A. A., Montmessin, F., Rodin, A. V., Korablev, O. I., Määttä, A., Maltagliati, L., & Bertaux, J. L. (2014). Evidence for a bimodal size distribution for the suspended aerosol particles on Mars. *Icarus*, *231*, 239–260. <https://doi.org/10.1016/j.icarus.2013.12.015>

Forget, F., Hourdin, F., Fournier, R., Hourdin, C., Talagrand, O., Collins, M., et al. (1999). Improved general circulation models of the Martian atmosphere from the surface to above 80 km. *Journal of Geophysical Research*, *104*(E10), 24155–24175. <https://doi.org/10.1029/1999je001025>

Gary-Bicas, C. E., Hayne, P. O., Horvath, T., Heavens, N. G., Kass, D. M., Kleinböhl, A., et al. (2020). Asymmetries in snowfall, emissivity, and albedo of Mars' seasonal polar caps: Mars climate sounder observations. *Journal of Geophysical Research: Planets*, *125*(5), e2019JE006150. <https://doi.org/10.1029/2019JE006150>

Gordon, I. E., Rothman, L. S., Hill, C., Kochanov, R. V., Tan, Y., Bernath, P. F., et al. (2017). The HITRAN2016 molecular spectroscopic database. *Journal of Quantitative Spectroscopy and Radiative Transfer*, *203*, 3–69. <https://doi.org/10.1016/j.jqsrt.2017.06.038>

Guzewich, S. D., Lemmon, M., Smith, C. L., Martínez, G., de Vicente-Retortillo, A., Newman, C. E., et al. (2019). Mars science laboratory observations of the 2018/Mars Year 34 global dust storm. *Geophysical Research Letters*, *46*(1), 71–79. <https://doi.org/10.1029/2018GL080839>

Guzewich, S. D., & Smith, M. D. (2019). Seasonal variation in Martian water ice cloud particle size. *Journal of Geophysical Research: Planets*, *124*(2), 636–643. <https://doi.org/10.1029/2018JE005843>

R. M. Haberle, R. T. Clancy, F. Forget, M. D. Smith, & R. W. Zurek (Eds.) (2017). *The atmosphere and climate of Mars*. Cambridge University Press. <https://doi.org/10.1017/9781139060172>

Hansen, J. E., & Travis, L. D. (1974). Light scattering in planetary atmospheres. *Space Science Reviews*, *16*(4), 527–610. <https://doi.org/10.1007/BF00168069>

Hayne, P. O., Paige, D. A., Schofield, J. T., Kass, D. M., Kleinböhl, A., Heavens, N. G., & McCleese, D. J. (2012). Carbon dioxide snow clouds on Mars: South polar winter observations by the Mars Climate Sounder. *Journal of Geophysical Research*, *117*(E8), E08014. <https://doi.org/10.1029/2011JE004040>

Jiménez-Monferrer, S., López-Valverde, M. A., Funke, B., González-Galindo, F., Piccialli, A., García-Comas, M., et al. (2021). CO₂ retrievals in the Mars daylight thermosphere from its 4.3 μm limb emission measured by OMEGA/MEX. *Icarus*, *353*, 113830. <https://doi.org/10.1016/j.icarus.2020.113830>

Kahre, M. A., Murphy, J. R., Newman, C. E., Wilson, R. J., Cantor, B. A., Lemmon, M. T., & Wolff, M. J. (2017). The Mars dust cycle. In F. Forget, M. D. Smith, R. T. Clancy, R. W. Zurek, & R. M. Haberle (Eds.), *The atmosphere and climate of Mars* (pp. 295–337). Cambridge University Press. <https://doi.org/10.1017/9781139060172.010>

Kass, D. M., Kleinböhl, A., McCleese, D. J., Schofield, J. T., & Smith, M. D. (2016). Interannual similarity in the Martian atmosphere during the dust storm season. *Geophysical Research Letters*, *43*(12), 6111–6118. <https://doi.org/10.1002/2016GL068978>

Kass, D. M., Schofield, J. T., Kleinböhl, A., McCleese, D. J., Heavens, N. G., Shirley, J. H., & Steele, L. J. (2020). Mars climate sounder observations of Mars' 2018 global dust storm. *Geophysical Research Letters*, *47*(23), e2019GL083931. <https://doi.org/10.1029/2019GL083931>

Kieffer, H. H., Titus, T. N., Mullins, K. F., & Christensen, P. R. (2000). Mars south polar spring and summer behavior observed by TES: Seasonal cap evolution controlled by frost grain size. *Journal of Geophysical Research*, *105*(E4), 9653–9699. <https://doi.org/10.1029/1999JE001136>

- Kleinböhl, A., Schofield, J. T., Abdou, W. A., Irwin, P. G. J., & de Kok, R. J. (2011). A single-scattering approximation for infrared radiative transfer in limb geometry in the Martian atmosphere. *Journal of Quantitative Spectroscopy and Radiative Transfer*, *112*(10), 1568–1580. <https://doi.org/10.1016/j.jqsrt.2011.03.006>
- Kleinböhl, A., Schofield, J. T., Kass, D. M., Abdou, W. A., Backus, C. R., Sen, B., et al. (2009). Mars Climate Sounder limb profile retrieval of atmospheric temperature, pressure, and dust and water ice opacity. *Journal of Geophysical Research*, *114*(E10), E10006. <https://doi.org/10.1029/2009JE003358>
- Korablev, O., Montmessin, F., Trokhimovskiy, A., Fedorova, A. A., Shakun, A. V., Grigoriev, A. V., et al. (2017). The atmospheric chemistry suite (ACS) of three spectrometers for the ExoMars 2016 trace gas orbiter. *Space Science Reviews*, *214*(1), 7. <https://doi.org/10.1007/s11214-017-0437-6>
- Kuroda, T., Medvedev, A. S., Kasaba, Y., & Hartogh, P. (2013). Carbon dioxide ice clouds, snowfalls, and baroclinic waves in the northern winter polar atmosphere of Mars. *Geophysical Research Letters*, *40*(8), 1484–1488. <https://doi.org/10.1002/grl.50326>
- Lee, C., Lawson, W. G., Richardson, M. I., Heavens, N. G., Kleinböhl, A., Banfield, D., et al. (2009). Thermal tides in the Martian middle atmosphere as seen by the Mars Climate Sounder. *Journal of Geophysical Research*, *114*(E3), E03005. <https://doi.org/10.1029/2008JE003285>
- Liuzzi, G., Villanueva, G. L., Crismani, M. M., Smith, M. D., Mumma, M. J., Daerden, F., et al. (2020). Strong variability of Martian water ice clouds during dust storms revealed from ExoMars trace gas orbiter/NOMAD. *Journal of Geophysical Research: Planets*, *125*(4), e2019JE006250. <https://doi.org/10.1029/2019JE006250>
- López Valverde, M.-A., Funke, B., Brines, A., Stolzenbach, A., Modak, A., Hill, B., et al. (2022). Martian atmospheric temperature and density profiles during the 1st year of NOMAD/TGO solar occultation measurements. *Journal of Geophysical Research: Planets*, e2022JE007278. <https://doi.org/10.1029/2022JE007278>
- Luginin, M., Fedorova, A., Belyaev, D., Montmessin, F., Wilquet, V., Korablev, O., et al. (2016). Aerosol properties in the upper haze of Venus from SPICAV IR data. *Icarus*, *277*, 154–170. <https://doi.org/10.1016/j.icarus.2016.05.008>
- Luginin, M., Fedorova, A., Ignatiev, N., Trokhimovskiy, A., Shakun, A., Grigoriev, A., et al. (2020). Properties of water ice and dust particles in the atmosphere of Mars during the 2018 global dust storm as inferred from the atmospheric chemistry suite. *Journal of Geophysical Research: Planets*, *125*(11), e2020JE006419. <https://doi.org/10.1029/2020JE006419>
- Madeleine, J.-B., Forget, F., Spiga, A., Wolff, M. J., Montmessin, F., Vincendon, M., et al. (2012). Aphelion water-ice cloud mapping and property retrieval using the OMEGA imaging spectrometer onboard Mars Express. *Journal of Geophysical Research*, *117*(E11), E00J07. <https://doi.org/10.1029/2011JE003940>
- Martin, L. J., & Zurek, R. W. (1993). An analysis of the history of dust activity on Mars. *Journal of Geophysical Research*, *98*(E2), 3221–3246. <https://doi.org/10.1029/92JE02937>
- Mishchenko, M. I., Travis, L. D., & Lacis, A. A. (2002). *Scattering, absorption, and emission of light by small particles*. Cambridge University Press.
- Modak, A., López-Valverde, M. A., Brines, A., Stolzenbach, A., Funke, B., González-Galindo, F., et al. (2023). Retrieval of Martian atmospheric CO vertical profiles from NOMAD observations during the 1st year of TGO operations. *Journal of Geophysical Research: Planets*, *128*(3), e2022JE007282. <https://doi.org/10.1029/2022je007282>
- Montmessin, F., Forget, F., Rannou, P., Cabane, M., & Haberle, R. M. (2004). Origin and role of water ice clouds in the Martian water cycle as inferred from a general circulation model. *Journal of Geophysical Research*, *109*(E10), E10004. <https://doi.org/10.1029/2004JE002284>
- Montmessin, F., Gondet, B., Bibring, J.-P., Langevin, Y., Drossart, P., Forget, F., & Fouchet, T. (2007). Hyperspectral imaging of convective CO₂ ice clouds in the equatorial mesosphere of Mars. *Journal of Geophysical Research*, *112*(E11), E11S90. <https://doi.org/10.1029/2007JE002944>
- Montmessin, F., Korablev, O., Lefèvre, F., Bertaux, J. L., Fedorova, A., Trokhimovskiy, A., et al. (2017). SPICAM on Mars Express: A 10 year in-depth survey of the Martian atmosphere. *Icarus*, *297*, 195–216. <https://doi.org/10.1016/j.icarus.2017.06.022>
- Montmessin, F., Rannou, P., & Cabane, M. (2002). New insights into Martian dust distribution and water-ice cloud microphysics. *Journal of Geophysical Research*, *107*(E6), 4–1–4–14. <https://doi.org/10.1029/2001JE001520>
- Navarro, J., & Aythami, A. (2016). *Retrieval of CO₂ and collisional parameters from the MIPAS spectra in the earth atmosphere*. Universidad de Granada. Retrieved from <https://digibug.ugr.es/handle/10481/41725> (Accepted: 2016-06-14T08:00:44Z Journal Abbreviation: Inversión del CO₂ y de parámetros colisionales de los espectros de MIPAS en la atmósfera terrestre).
- Navarro, T., Forget, F., Millour, E., & Greybush, S. J. (2014). Detection of detached dust layers in the Martian atmosphere from their thermal signature using assimilation. *Geophysical Research Letters*, *41*(19), 6620–6626. <https://doi.org/10.1002/2014GL061377>
- Neary, L., Daerden, F., Aoki, S., Whiteway, J., Clancy, R. T., Smith, M., et al. (2020). Explanation for the increase in high-altitude water on Mars observed by NOMAD during the 2018 global dust storm. *Geophysical Research Letters*, *47*(7), e2019GL084354. <https://doi.org/10.1029/2019GL084354>
- Powell, M. J. (1970). A hybrid method for nonlinear equations. *Numerical methods for nonlinear algebraic equations*.
- Richardson, M. I., & Wilson, R. J. (2002). Investigation of the nature and stability of the Martian seasonal water cycle with a general circulation model. *Journal of Geophysical Research*, *107*(E5), 7–1–7–28. <https://doi.org/10.1029/2001JE001536>
- Rodgers, C. D. (2000). *Inverse methods for atmospheric sounding*. World Scientific. <https://doi.org/10.1142/3171>
- Sánchez-Lavega, A., del Río-Gaztelurrutia, T., Hernández-Bernal, J., & Delcroix, M. (2019). The onset and growth of the 2018 Martian global dust storm. *Geophysical Research Letters*, *46*(11), 6101–6108. <https://doi.org/10.1029/2019GL083207>
- Shirley, J. H., Kleinböhl, A., Kass, D. M., Steele, L. J., Heavens, N. G., Suzuki, S., et al. (2020). Rapid expansion and evolution of a regional dust storm in the Acidalia corridor during the initial growth phase of the Martian global dust storm of 2018. *Geophysical Research Letters*, *47*(9), e2019GL084317. <https://doi.org/10.1029/2019GL084317>
- Smith, M. D. (2004). Interannual variability in TES atmospheric observations of Mars during 1999–2003. *Icarus*, *167*(1), 148–165. <https://doi.org/10.1016/j.icarus.2003.09.010>
- Smith, M. D. (2019). THEMIS observations of the 2018 Mars global dust storm. *Journal of Geophysical Research: Planets*, *124*(11), 2929–2944. <https://doi.org/10.1029/2019JE006107>
- Smith, M. D., Wolff, M. J., Clancy, R. T., Kleinböhl, A., & Murchie, S. L. (2013). Vertical distribution of dust and water ice aerosols from CRISM limb-geometry observations. *Journal of Geophysical Research: Planets*, *118*(2), 321–334. <https://doi.org/10.1002/jgre.20047>
- Smith, M. D., Wolff, M. J., Spanovich, N., Ghosh, A., Banfield, D., Christensen, P. R., et al. (2006). One Martian year of atmospheric observations using MER Mini-TES. *Journal of Geophysical Research*, *111*(E12), E12S13. <https://doi.org/10.1029/2006JE002770>
- Sorensen, D. C. (1982). Newton's method with a model trust region modification. *SIAM Journal on Numerical Analysis*, *19*(2), 409–426. <https://doi.org/10.1137/0719026>
- Stcherbinine, A., Vincendon, M., Montmessin, F., Wolff, M. J., Korablev, O., Fedorova, A., et al. (2020). Martian water ice clouds during the 2018 global dust storm as observed by the ACS-MIR channel onboard the trace gas orbiter. *Journal of Geophysical Research: Planets*, *125*(3), e2019JE006300. <https://doi.org/10.1029/2019JE006300>

- Stiller, G. P., Hoepfner, M., Kuntz, M., von Clarmann, T., Echele, G., Fischer, H., et al. (1998). Karlsruhe optimized and precise radiative transfer algorithm: I. Requirements, justification, and model error estimation. In J. Wang, B. Wu, T. Ogawa, & Z. Hua Guan (Eds.), *Optical remote sensing of the atmosphere and clouds* (Vol. 3501, pp. 257–268). SPIE. <https://doi.org/10.1117/12.317754>
- Stolzenbach, A. (2023). ADS v4 results for MY 34 & 35 [Dataset]. Zenodo. <https://doi.org/10.5281/zenodo.7753821>
- Stolzenbach, A., Valverde, M.-A. L., Brines, A., Modak, A., Funke, B., González-Galindo, F., et al. (2023). Martian atmospheric aerosols composition and distribution retrievals during the first Martian year of NOMAD/TGO solar occultation measurements. Part II: Extended results, end of MY 34 and first half of MY 35.
- Trompet, L., Vandaele, A., Thomas, I., Aoki, S., Daerden, F., Erwin, J., et al. (2023). Carbon dioxide retrievals from NOMAD-SO on ESA's ExoMars trace gas orbiter and temperature profiles retrievals with the hydrostatic equilibrium equation. I. Description of the method. *Journal of Geophysical Research: Planets*, 128(3), e2022JE007277. <https://doi.org/10.1029/2022je007277>
- Vago, J., Witasse, O., Svedhem, H., Baglioni, P., Haldemann, A., Gianfiglio, G., et al. (2015). ESA ExoMars program: The next step in exploring Mars. *Solar System Research*, 49(7), 518–528. <https://doi.org/10.1134/S0038094615070199>
- Vandaele, A. C., Lopez-Moreno, J.-J., Patel, M. R., Bellucci, G., Daerden, F., Ristic, B., et al. (2018). NOMAD, an integrated suite of three spectrometers for the ExoMars trace gas mission: Technical description, science objectives and expected performance. *Space Science Reviews*, 214(5), 80. <https://doi.org/10.1007/s11214-018-0517-2>
- Vandaele, A. C., Neefs, E., Drummond, R., Thomas, I. R., Daerden, F., Lopez-Moreno, J. J., et al. (2015). Science objectives and performances of NOMAD, a spectrometer suite for the ExoMars TGO mission. *Planetary and Space Science*, 119, 233–249. <https://doi.org/10.1016/j.pss.2015.10.003>
- Villanueva, G. L., Liuzzi, G., Aoki, S., Stone, S. W., Brines, A., Thomas, I. R., et al. (2022). The deuterium isotopic ratio of water released from the Martian caps as measured with TGO/NOMAD. *Geophysical Research Letters*, 49(12), e2022GL098161. <https://doi.org/10.1029/2022gl098161>
- Virtanen, P., Gommers, R., Oliphant, T. E., Haberland, M., Reddy, T., Cournapeau, D., et al. (2020). SciPy 1.0: Fundamental algorithms for scientific computing in Python. *Nature Methods*, 17(3), 261–272. <https://doi.org/10.1038/s41592-019-0686-2>
- Voglis, C., & Lagaris, I. (2019). A rectangular trust-region approach for unconstrained and box-constrained optimization problems. In *International conference of computational methods in sciences and engineering 2004 (ICCMSE 2004)* (pp. 562–565).
- von Clarmann, T., Glatthor, N., Grabowski, U., Höpfner, M., Kellmann, S., Kiefer, M., et al. (2003). Retrieval of temperature and tangent altitude pointing from limb emission spectra recorded from space by the Michelson Interferometer for Passive Atmospheric Sounding (MIPAS). *Journal of Geophysical Research*, 108(D23), 4736. <https://doi.org/10.1029/2003JD003602>
- Warren, S. G., & Brandt, R. E. (2008). Optical constants of ice from the ultraviolet to the microwave: A revised compilation. *Journal of Geophysical Research*, 113(D14), D14220. <https://doi.org/10.1029/2007JD009744>
- Wilson, R. J., Lewis, S. R., Montabone, L., & Smith, M. D. (2008). Influence of water ice clouds on Martian tropical atmospheric temperatures. *Geophysical Research Letters*, 35(7), L07202. <https://doi.org/10.1029/2007GL032405>
- Wolff, M. J., & Clancy, R. T. (2003). Constraints on the size of Martian aerosols from Thermal Emission Spectrometer observations. *Journal of Geophysical Research*, 108(E9), 5097. <https://doi.org/10.1029/2003JE002057>
- Wolff, M. J., López-Valverde, M., Madeleine, J.-B., Wilson, R. J., Smith, M. D., Fouchet, T., & Delory, G. T. (2017). Radiative process: Techniques and applications. In F. Forget, M. D. Smith, R. T. Clancy, R. W. Zurek, & R. M. Haberle (Eds.), *The atmosphere and climate of Mars* (pp. 106–171). Cambridge University Press. <https://doi.org/10.1017/9781139060172.006>
- Wolff, M. J., Smith, M. D., Clancy, R. T., Arvidson, R., Kahre, M., Seelos IV, F., et al. (2009). Wavelength dependence of dust aerosol single scattering albedo as observed by the Compact Reconnaissance Imaging Spectrometer. *Journal of Geophysical Research*, 114(E2), E00D04. <https://doi.org/10.1029/2009JE003350>
- Wolff, M. J., Smith, M. D., Clancy, R. T., Spanovich, N., Whitney, B. A., Lemmon, M. T., et al. (2006). Constraints on dust aerosols from the Mars Exploration Rovers using MGS overflights and Mini-TES. *Journal of Geophysical Research*, 111(E12), E12S17. <https://doi.org/10.1029/2006JE002786>